Published in final edited form as:
Geochim Cosmochim Acta. 2019 October 15; 263: 215–234. doi:10.1016/j.gca.2019.07.021.

Combined mass-dependent and nucleosynthetic isotope variations in refractory inclusions and their mineral separates to determine their original Fe isotope compositions

Quinn R. Shollenberger[a,*], **Andreas Wittke**[b], **Jan Render**[a], **Prajkta Mane**[c], **Stephan Schuth**[d], **Stefan Weyer**[d], **Nikolaus Gussone**[b], **Meenakshi Wadhwa**[c], **Gregory A. Brennecka**[a]

[a]Institut für Planetologie, University of Münster, Wilhelm-Klemm-Straße 10, 48149 Münster, Germany.

[b]Institut für Mineralogie, University of Münster, Corrensstraße 24, 48149 Münster, Germany.

[c]School of Earth and Space Exploration, Arizona State University, PO Box 871404, Tempe, AZ 85287-1404 USA.

[d]Institut für Mineralogie, Leibniz University Hannover, Callinstraße 3, 30167 Hannover, Germany.

Abstract

Calcium-aluminum-rich inclusions (CAIs) are the oldest dated materials that provide crucial information about the isotopic reservoirs present in the early Solar System. For a variety of elements, CAIs have isotope compositions that are uniform yet distinct from later formed solid material. However, despite being the most abundant metal in the Solar System, the isotopic composition of Fe in CAIs is not well constrained. In an attempt to determine the Fe isotopic compositions of CAIs, we combine extensive work from a previously studied CAI sample set with new isotopic work characterizing mass-dependent and mass-independent (nucleosynthetic) signatures in Mg, Ca, and Fe. This investigation includes work on three mineral separates of the Allende CAI Egg 2. For all isotope systems investigated, we find that in general, fine-grained CAIs exhibit light mass-dependent isotopic signatures relative to terrestrial standards, whereas igneous CAIs have heavier isotopic compositions relative to the fine-grained CAIs. Importantly, the mass-dependent Fe isotope signatures of bulk CAIs show a range of both light (fine-grained CAIs) and heavy (igneous CAIs) isotopic signatures relative to bulk chondrites, suggesting that Fe isotope signatures in CAIs largely derive from mass fractionation events such as condensation and evaporation occurring in the nebula. Such signatures show that a significant portion of the secondary alteration experienced by CAIs, particularly prevalent in fine-grained inclusions, occurred in the nebula prior to accretion into their respective parent bodies.

Regarding nucleosynthetic Fe isotope signatures, we do not observe any variation outside of analytical uncertainty in bulk CAIs compared to terrestrial standards. In contrast, all three Egg 2 mineral separates display resolved mass-independent excesses in ^{56}Fe compared to terrestrial standards. Furthermore, we find that the combined mass-dependent and nucleosynthetic Fe isotopic compositions of the Egg 2 mineral separates are well correlated, likely indicating that Fe indigenous to the CAI is mixed with less anomalous Fe, presumably from the solar nebula. Thus,

*Corresponding author shollenberger@wwu.de, phone: +49 251 83 36377, fax: +49 251 83 3601.

these reported nucleosynthetic anomalies may point in the direction of the original Fe isotope composition of the CAI-forming region, but they likely only provide a minimum isotopic difference between the original mass-independent Fe isotopic composition of CAIs and that of later formed solids.

1. INTRODUCTION

Marking the start of our Solar System, calcium-aluminum-rich inclusions (CAIs) are the oldest dated solids that formed at about 4.567 Ga (Amelin et al., 2010; Bouvier et al., 2011a; Connelly et al., 2012). Therefore, CAIs provide insightful information about the starting materials and processing of the earliest reservoir(s) in the Solar System. For example, the petrology and chemical make-up of a CAI may reveal the formation conditions and subsequent processes that acted on that sample, whereas the isotopic composition of a CAI can identify its original starting material and subsequent mixing with other reservoirs. The natural isotope variations of CAIs may reflect mass-independent processes which include 1) radiogenic ingrowth, 2) nuclear transmutations caused by irradiation, or 3) nucleosynthetic anomalies arising from the incomplete homogenization of presolar material. In contrast, mass-dependent isotope variations record physicochemical processes such as evaporation or condensation, or in some cases, isotopic fractionation caused by redox transitions. Importantly, it has been well-documented that CAIs have both mass-dependent and mass-independent (nucleosynthetic) isotopic anomalies relative to later formed solids such as chondrules, chondrites, and terrestrial planets (see review by Dauphas and Schauble, 2016, and references therein). The most isotopically distinct subgroups of CAIs are the hibonite-rich inclusions (distinguished mineralogically as platy hibonite crystals (PLACs) and spinel-hibonite inclusions (SHIBs)) and the rare FUN (Fractionation and Unknown Nuclear effects) inclusions (*e.g.*, Krot et al., 2014; Kööp et al., 2016). The FUN CAIs in particular display the largest mass-dependent effects as well as large nucleosynthetic anomalies. However, this study focuses on CAIs from CV3 and CK3 chondrites (hereafter referred to simply as CAIs) that typically display smaller mass-dependent isotope fractionations and isotope anomalies than FUN CAIs.

Many prior studies of CAIs focusing on nucleosynthetic isotopic variations have targeted elements in and around the Fe-peak of nucleosynthesis such as Ca, Ti, Cr, Ni, and Zn (*e.g.*, Clayton and Mayeda, 1977; Wasserburg et al., 1977; Niederer et al., 1980, 1981, 1985; Niemeyer and Lugmair, 1981; Heydegger et al., 1982; Niederer and Papanastassiou, 1984; Birck and Allègre, 1984, 1985; Birck and Lugmair, 1988; Papanastassiou and Brigham, 1989; Loss and Lugmair, 1990; Quitté et al., 2007; Leya et al., 2009; Chen et al., 2009; Trinquier et al., 2009; Huang et al., 2012; Williams et al., 2016; Simon et al., 2017; Davis et al., 2018; Bermingham et al., 2018; Render et al., 2018). In general, these studies report that CAIs have nucleosynthetic signatures for these elements that are distinct from terrestrial compositions, and they typically have the largest anomaly in the most neutron-rich isotopes of these elements (*i.e.*, ^{48}Ca, ^{50}Ti, ^{54}Cr, ^{64}Ni). Correlations in isotopes of different elements in and around the Fe-peak (*i.e.*, Sc to Ge) can help to identify nucleosynthetic sources that contributed to the solar nebula and can, thus, aid in understanding the late evolution of stars. For example, Nittler et al. (2018) reported correlated ^{54}Cr and ^{50}Ti anomalies in presolar

oxide grains, suggesting that these grains likely formed in Type Ia supernovae (SN Ia) or electron-capture supernovae. Therefore, if nucleosynthetic correlations such as these are present in CAIs, this may aid in understanding why the reservoir from which CAIs formed was isotopically distinct. However, while many elements in and around the Fe-peak have been studied comprehensively, the Fe isotopic composition of CAIs has not been investigated extensively to date.

Iron is an interesting element for isotopic investigation because it has four stable isotopes, ^{54}Fe (5.845%), ^{56}Fe (91.754%), ^{57}Fe (2.119%), and ^{58}Fe (0.282%) that are produced by nuclear statistical equilibrium, also called the e-process of nucleosynthesis (*e.g.*, Hainebach et al., 1974). Depending on the type of stellar environment (*e.g.*, its mass, neutron density, or location within the stellar source), these isotopes can be expected to be over- or under-produced relative to terrestrial isotope abundances. However, despite being the most abundant metal in the Solar System, the isotopic composition of Fe in CAIs is not well constrained as only one study to date has investigated the mass-independent Fe isotope compositions of CAIs (Völkening and Papanastassiou, 1989). They reported Fe isotope variability in two FUN CAIs and in addition, they reported that the Allende CAI Egg 2 is characterized by a small deficit in ^{57}Fe and a large excess in the neutron-rich isotope ^{58}Fe. However, the same study also measured three other non-FUN CAI samples which did not have resolved excesses in ^{58}Fe, suggesting that Egg 2 may be a unique sample.

Compared to elements in CAIs like Al and Ca, Fe is not predicted to be a major constituent of CAIs due to its lower condensation temperature and the highly reduced conditions of CAI formation. However, Fe can replace other elements (*i.e.*, Mg, Ca) during secondary alteration. For example, it is well-documented in CAIs that MgO is replaced by FeO and ZnO within spinel during secondary alteration (*e.g.,* Rout and Bischoff, 2008). Furthermore, perovskite, a typical mineral found in CAIs, can be fully or partially converted to ilmenite during secondary alteration resulting from FeO replacing CaO (*e.g.*, Bischoff and Keil 1984). With such potential for pervasive Fe replacement, obtaining a robust pre-alteration isotopic signature of Fe in CAIs is not straightforward. Therefore, in this work we attempt to decipher the original Fe isotopic composition of the CAI-forming region by examining the Fe isotopic compositions in a large, well-characterized CAI sample set along with separated mineral phases from the Egg 2 CAI.

In contrast to nucleosynthetic effects—which probe the original building material of CAIs—multiple studies have investigated the mass-dependent Mg, Ca, Ti, and Ni isotopic signatures in CAIs. This is done to understand the processes involved in CAI formation such as evaporation and condensation or isotopic exchange with later formed solids (*e.g.*, Lee et al., 1979; Niederer and Papanastassiou, 1984; Bizzarro et al., 2004; Huang et al., 2012; Schiller et al., 2015, 2016; Amsellem et al., 2017; Davis et al., 2018; Simon et al., 2017; Bermingham et al., 2018; Render et al., 2018). Although the Fe mass-dependent signatures of CAIs could indicate their condensation/evaporation histories, only two studies have examined mass-dependent Fe isotopic compositions in CAIs (Mullane et al., 2005; Hezel et al., 2008). These studies found that most CAIs measured were isotopically light in their Fe composition compared to bulk chondrite and terrestrial values; however, the interpretation of

these signatures is not straightforward, as Fe is susceptible to secondary alteration in CAIs. Thus, the mass-dependent Fe isotope compositions of CAIs remains poorly constrained.

This study seeks to investigate the original Fe isotopic composition of the CAI-forming region by examining the mass-dependent and nucleosynthetic isotopic signatures of a variety of elements (*i.e.*, Mg, Ca, Ti, Fe, Ni, Sr, U) using a well-studied CAI sample set (Burkhardt et al., 2008; Brennecka et al., 2010; Kruijer et al., 2014; Shollenberger et al., 2018). This sample set includes CAIs with large excesses in the most neutron-rich isotopes of Ti, Cr, and Ni (Mercer et al., 2015; Brennecka et al., 2017b; Render et al., 2018). Additionally, we revisit the Allende CAI Egg 2, the sample with the reported large mass-independent excess in ^{58}Fe (Völkening and Papanastassiou, 1989), by investigating three mineral separates from the same sample, which may aid in separating and distinguishing between the primary and secondary Fe hosted in this inclusion.

2. SAMPLES AND METHODS

2.1 Samples investigated

The samples selected for this study were previously digested CAIs that have mass-dependent and nucleosynthetic anomalies in many other elements such as Ti, Cr, Ni, Zr, Sr, Mo, Ba, Nd, Sm, Er, Yb, Hf, and U (*e.g.*, Burkhardt et al., 2008; Brennecka et al., 2010; Kruijer et al., 2014; Shollenberger et al., 2018; Render et al., 2018) along with three mineral separates from an aliquot of the Egg 2 CAI provided by the late G. J. Wasserburg. The mineral separation of Egg 2, a type B CAI from the Allende CV3.6 chondrite, was done at the California Institute of Technology mainly by heavy liquid separation (methylene iodide and acetone) followed by magnetic susceptibility separation. The separated phases were divided into three groups, namely 3.3 g/mL sink – magnetic (89 mg), 3.3 g/mL sink – less magnetic (38 mg), and 3.1 g/mL float (55 mg), which broadly represent high-Fe pyroxene (high-Fe Px), high-Mg pyroxene (high-Mg Px), and plagioclase (Plag) separates, respectively. Following transfer to Arizona State University (ASU), the separates of Egg 2 were exposed to a combination of concentrated HF, HNO_3, and HCl to achieve total sample dissolution.

Detailed sample information about the bulk CAIs can be found in the aforementioned studies, but a brief overview of all the samples is given in Table 1. This sample set of 26 bulk CAIs includes multiple petrologic types of CAIs (A, B, and C) and samples that have experienced different thermal histories, as evidenced by their varied REE patterns (Fig. 1a). The heavy rare earth element (HREE) patterns of the mineral separates from the Egg 2 type B Allende CAI (Fig. 1b) are relatively unfractionated. The Egg 2 pyroxene separates have light rare earth element (LREE) depletions and negative Eu anomalies characteristic of this phase, while the Egg 2 plagioclase has a slight LREE enrichment and positive Eu anomaly that is typical for this mineral. A calculated bulk Egg 2 REE pattern is also flat with a negative Eu anomaly, consistent with a group I/III pattern. For consistency, throughout this work the term *igneous* is used to describe relatively coarse-grained CAIs of the type A, B, or C, whereas the remaining CAIs are designated as *fine-grained*, which includes an altered type A inclusion and a fluffy type A inclusion (Table 1). The terrestrial rock standards BCR-2 and BHVO-2 along with an aliquot of bulk Allende were also included in this study

to verify analytical procedures. Note that all systems previously investigated for each sample are given below in Table 1.

2.2 Trace element measurements

Sample solution aliquots, prior to any chemical separations, were measured for trace element abundances and reported in previous studies (see Table 1) for most of the bulk CAIs in this work (Brennecka et al., 2010; Kruijer et al., 2014; Shollenberger et al., 2018a). The details of trace element measurements for CAIs from Burkhardt et al. (2008) are found in Burkhardt et al. (2012). For the Egg 2 separates, an aliquot (~1%) of each initial sample dissolution was reserved for trace element analyses by quadrupole ICPMS (Thermo Scientific® XSERIES) at ASU (REE patterns provided in Fig 1b). All REE data from samples utilized in this study are given in the electronic annex.

2.3 Chemical separation and isotope measurements of Mg, Ca, Ti, Fe, Ni, Sr, and U

Presented below are the chemical separation procedures and mass spectrometry methods used to isolate, purify, and measure all elements investigated in this study. Sample solution aliquots for each element were taken from minimally processed materials (see electronic annex for concerns regarding previous chemical procedures). All chemical reagents used in this study were standard clean lab acids (*e.g.*, Merck Millipore Emsure™ grade acids (69% HNO_3, 37% HCl, 48% HF) that had been distilled twice with Savillex™ DST-1000 Acid Purification Systems) and were diluted appropriately with 18.2 MΩ* cm H_2O (Millipore Milli-Q®, hereafter “MQ”). Throughout this study, all mass-dependent variations are presented in δ-notation, or deviation from the terrestrial standard in parts per thousand using the following equation where E is the element of interest (*e.g.*, Fe), *i* is the isotope of interest (*e.g.*, ^{56}Fe), and *j* is the reference isotope (*e.g.*, ^{54}Fe):

$$\delta^{i}E_{sample} = \left(\frac{(^{i}E\ /\ ^{j}E)_{sample}}{(^{i}E\ /\ ^{j}E)_{standard}} - 1\right) \times 1,000$$

In contrast, after correction for mass-dependent effects all nucleosynthetic variations are shown in ε-notation, or mass-independent deviations from the terrestrial standard in parts per ten thousand using the following equation:

$$\varepsilon^{i}X_{sample} = \left(\frac{(^{i}X\ /\ ^{j}X)_{sample}}{(^{i}X\ /\ ^{j}X)_{standard}} - 1\right) \times 10,000$$

In this equation, X is the element of interest (*e.g.*, Fe), *i* is the isotope of interest (*e.g.*, ^{58}Fe), and *j* is the isotope in the denominator of the internal normalization ratio (*e.g.*, ^{54}Fe). Furthermore, the nucleosynthetic variations are determined by internally normalizing to a fixed isotope ratio using the exponential law to cancel out instrumental mass bias and natural stable isotope fractionation (see details for each element below). The reported uncertainties represent the 2× standard deviation (2SD) of replicate sample analyses or the long-term reproducibility of the terrestrial standard (*i.e.*, 2SD of repeat analyses of the terrestrial standard) during the measurement campaign.

2.3.1 Magnesium—Chemical separation of Mg took place in the Isotope Cosmochemistry and Geochronology Laboratory (ICGL) at ASU using procedures adapted from Spivak-Birndorf et al. (2009) and Bouvier et al. (2011b). Approximately 5% of each dissolved CAI sample (equivalent to ~6-16 μg Mg) was passed through a cation-exchange column packed with AG50x8 200-400 mesh resin, and Mg was eluted in 1 N HNO_3. This column procedure was repeated three times for each sample to ensure complete separation of Mg from Al, Ca, and other cations (*i.e.*, Fe, Na), and resulted in recovery of >98% of the Mg for each sample. Magnesium isotopic analysis was performed on the Thermo Scientific® Neptune MC-ICPMS housed in the ICGL at ASU. The purified Mg samples, diluted to 250 ppb Mg in 3% HNO_3, were introduced into the mass spectrometer with a flow rate of 100 μL/min using an ESI APEX® desolvating nebulizer system achieving a beam intensity of ~22-25 V on ^{24}Mg. The mass spectrometer was operated in medium resolution mode in order to separate molecular interferences of $^{12}C2^{+}$, $^{12}C^{14}N^{+}$, and $^{24}MgH^{+}$. The instrumental mass bias was corrected using the sample-standard bracketing method, using the Mg isotopic standard DSM-3. An individual measurement consisted of 20 cycles utilizing 8 s integration times, and samples were measured three times each. The external reproducibility (2SD) in this work was ±0.07 for $\delta^{25/24}Mg$ and ±0.11 for $\delta^{26/24}Mg$.

2.3.2 Calcium—Chemical separation of Ca took place in the clean lab at the Institut für Mineralogie at the University Münster. For Ca purification, aliquots corresponding to 3 μg Ca were removed from dissolved mineral separates and CAI matrices. Calcium was purified from the rock matrix using the method of Ockert et al. (2013), in particular to remove K^{+} to avoid the isobaric interference of ^{40}K on ^{40}Ca. The aliquots were spiked with a $^{42}Ca/^{43}Ca$ double spike (Gussone et al., 2011) to correct for mass-dependent Ca isotope fractionation during isotope analysis (*e.g.*, Russell and Papanastassiou, 1978; Habfast, 1983; Hart and Zindler, 1989) and Ca purification during column chromatography (*e.g.*, Russell et al., 1978). Briefly, Teflon® columns were filled with pre-cleaned MCI Gel CK08P resin and conditioned with 1.8 N HCl. The samples were loaded onto the columns in 1.8 N HCl to execute ion chromatographic separation. The purified Ca was collected, evaporated, and recovered in 6 N HCl. Purified Ca cuts were loaded on outgassed Re single filaments with a TaF_5 activator solution using the sandwich technique with 0.5 μL TaF_5 solution, 1 μL sample solution, and 1 μL of TaF_5 solution (*e.g.*, Gussone et al., 2011). The samples were measured at least twice on two separate filaments with a Thermo Scientific® Triton housed in the Institut für Mineralogie at the University Münster. The $^{44}Ca/^{40}Ca$ of the sample was corrected for isotope fractionation during the evaporation in the ion source of the TIMS by an iterative approach using the exponential law based on the method described in Heuser et al. (2002). The samples were corrected for the ^{40}K interference by monitoring ^{41}K, although ^{40}K signals were negligible. The normalization standard in this work was SRM915a, and the external reproducibility (2SD) was $\pm 0.08\%_0$ for $5^{44/40}Ca$.

2.3.3 Titanium—Chemical separation of Ti occurred in the clean lab at the Institut für Planetologie at the University of Münster. Titanium was separated from the sample solution aliquot following a two-step ion-exchange chromatography procedure (Zhang et al., 2011). In short, samples were loaded onto columns containing 2 mL TODGA resin in 12 N HNO_3. The matrix was rinsed from the column in 12 N HNO_3 and Ti was eluted subsequently in 12

N HNO_3 – 1 wt% H_2O_2. The second column utilized 0.8 mL AG1-X8 (200-400 mesh) anion-exchange resin. The Ti fractions from the first column were dried down and then loaded in 4 N HF. The matrix was removed using 4 N HF and 0.4 N HCl – 1 N HF, before Ti was eluted in 9 N HCl – 0.01 N HF. The Ti isotopic compositions of the mineral separates were measured at the University of Münster using a Thermo Scientific® Neptune *Plus* MC-ICPMS in high-resolution mode following previously established methods (Zhang et al., 2011; Gerber et al., 2017). The Ti isotopic compositions were collected using a two-line data acquisition method. In the first line, all Ti isotopes were monitored along with ^{51}V and ^{53}Cr and were measured for 40 cycles utilizing 4 s integration times. For the second line, all Ti isotopes were measured along with ^{44}Ca in blocks of 20 cycles using 4 s integration times. Instrumental mass bias was corrected using the exponential law and normalizing to $^{49}Ti/^{47}Ti = 0.749766$ (Zhang et al., 2011), and Ti isotopic compositions are reported relative to the Origins Lab titanium (OL-Ti) bracketing standard (Millet and Dauphas, 2014). The external reproducibility (2SD) of the method is ±0.30 for $\varepsilon^{46}Ti$ and ±0.29 for $\varepsilon^{50}Ti$.

2.3.4 Iron—Chemical separation of Fe occurred in the clean lab at the Institut für Planetologie at the University of Münster. Sample dissolution aliquots corresponding to approximately 100 μg Fe were obtained for each CAI and mineral separate. Iron was separated from the sample matrix using ~1.8 mL AG1-X8 (100-200 mesh) anion-exchange resin following the procedure from Schuth et al. (2015). Briefly, the resin was cleaned with MQ H_2O, 3 N HNO_3, 0.4 N HCl, and 7 N HCl. Samples were loaded in 7 N HCl, and the columns were rinsed with 7 N HCl to remove the matrix. Subsequently, Fe was removed and collected from the column with MQ H_2O followed by 3 N HNO3. Then 100 μL 30% H_2O_2 was added to the Fe fractions and they were evaporated to dryness overnight. Multiple passes (2-3) through this procedure was sufficient to remove isobaric interferences (*e.g.*, Cr, Ni) that may affect Fe isotopic measurements. In preparation for mass spectrometry, the Fe fractions were treated with 500 μL concentrated HNO_3 and 50 μL of 30% H_2O_2 in order to remove any remaining organic compounds.

The Fe isotopic compositions of the samples and standards were measured on a Thermo Scientific® Neptune *Plus* MC-ICPMS in the Institut für Mineralogie at the Leibniz University Hannover, Germany. Samples and standards were measured in high mass resolution mode (mass resolving power of ~12,000) so as to fully resolve the Fe peaks from molecular interferences. To enable concurrent mass-dependent and internally normalized (mass-independent) data collection, a Cu solution (Alfa Aesar, Specpure) was added to the purified Fe aliquot of samples and standards prior to analyses to yield 2 ppm Cu. The use of Cu as an “element spike” to correct instrumental mass bias has been previously described (*e.g.*, Arnold et al., 2004; Weyer et al., 2005; Oeser et al., 2014; Schuth et al., 2015). To obtain Fe mass-dependent data (given in δ-notation), instrumental mass bias was corrected using external normalization and the exponential law ($^{63}Cu/^{65}Cu = 2.24359$, Berglund and Wieser 2011; Rosman and Taylor 1998). To obtain Fe mass-independent data (given in ε-notation), instrumental mass bias was corrected using the exponential law, normalizing to $^{57}Fe/^{54}Fe = 0.36255$ (Taylor et al., 1992). The commercially available IRMM-014 Fe reference material was also doped with Cu in the same way as the sample solutions. Samples were measured three times each using the following sequence: IRMM-014—sample1—

sample2—IRMM-014—sample3—sample4—IRMM-014. The isotope compositions of the samples are reported relative to the two bracketing IRMM-014 standards. Terrestrial rock standards and the in-house standard ETH Fe salt (from ETH Zürich, Switzerland) were also used to verify mass spectrometry procedures. All isotope beams were collected utilizing 10^{11} Ω resistors with the exception of ^{56}Fe, where a 10^{10} Ω resistor was used due to the higher signal for the most abundant isotope of Fe. An individual measurement consisted of 30 cycles using the cup configuration from Table 2. Using a two-line data acquisition method, Cu isotopes were collected using 4 s integration times and all four Fe isotopes along with the interference monitors ^{53}Cr and ^{60}Ni were collected using 8 s integration times. Samples and standards were matched in Fe concentration to be within ~10% of each other. Typical signal intensities on ^{56}Fe were around 35-50 V (on 10^{10} Ω resistor) for 6 to 8 ppm Fe solutions. Samples were measured during two different analytical sessions and the external reproducibility (2SD) of the IRMM-014 reference material during the two separate sessions was ±0.05 and ±0.08 for $\delta^{56/54}$Fe (mass-dependent). The 2SD of repeat analyses of the IRMM-014 reference material during two different measurement sessions was ±0.24 and ±0.29 for ε^{56}Fe and ±1.74 and ±1.46 for ε^{58}Fe (mass-independent). The electronic annex has more information regarding the precision and accuracy of our methods.

In this work, the mass-independent Fe isotopic compositions are internally normalized to a fixed isotope ratio ^{57}Fe/^{54}Fe as described above, resulting in any anomalies displayed as variations in ε^{56}Fe and ε^{58}Fe. This normalization scheme was used in previous studies (Dauphas et al., 2004; Cook and Schönbächler, 2017) and is the most favorable normalization scheme to show isotopic anomalies based on how the isotopes of Fe are created (see electronic annex). However, in order to directly compare our Egg 2 mineral separate data with a previous measurement of bulk Egg 2 (Völkening and Papanastassiou, 1989), the mass-independent Fe Egg 2 mineral separate data (*i.e.*, ε^{57}Fe and ε^{58}Fe values) were also obtained by using the exponential law to correct instrumental mass bias and normalizing to ^{56}Fe/^{54}Fe = 15.69786 (Rosman and Taylor, 1998).

2.3.5 Nickel—Chemical separation of Ni took place in the clean lab at the Institut für Planetologie at the University of Münster, following the procedure outlined in Render et al. (2018). Briefly, this purification procedure employs both cation- and anion-exchange resins, as well as various mixtures of HCl-acetone, HCl-acetic acid, and diluted HCl-HF and HNO_3-HF solutions. The entire chemical procedure usually results in yields >70% and a procedural blank of ~5 ng, which is negligible, considering over 1 μg Ni was processed per sample. Spiked Ni isotope measurements for the investigation of mass-dependent fractionation were performed using the Nu Plasma II MC-ICPMS at Indiana University in Bloomington, following the procedure of Wang and Wasylenki (2017). Using 350 ppb Ni solutions, this measurement setup yields an external reproducibility of ±0.06 (2SD) for $\delta^{60/58}$Ni in medium resolution mode. Double-spike deconvolution was performed using MATLAB and is described in detail in Wasylenki et al. (2014). Possible contributions on the mass-dependent isotopic signatures from non-terrestrial Ni isotope compositions (*i.e.*, nucleosynthetic isotope variation) were obtained using the internally normalized measurements (performed in the Institut für Planetologie at the University of Münster using a Thermo Scientific® Neptune *Plus* MC-ICPMS) of an unspiked solution of bulk Egg 2

(Render et al., 2018). This resulted in contributions of up to ~0.08‰, which is similar to the external reproducibility of our method and almost negligible compared to the degree of mass-dependent fractionation (*e.g.*, $\delta^{60/58}Ni_{measured}$ = +4.32; $\delta^{60/58}Ni_{corrected}$ = +4.24) seen in these samples. The external reproducibility (2SD) for the mass-independent Ni isotope compositions were ±0.08 for ε^{60}Ni, ±0.18 for ε^{62}Ni, and ±0.60 for ε^{64}Ni.

2.3.6 Strontium—Chemical separation of Sr occurred in the clean lab at the Institut für Planetologie at the University of Münster. Strontium was isolated from the mineral separate matrices based on the procedure from Carlson et al. (2007). Cation-exchange resin (AG50W-X8, 200-400 mesh) was used to elute Sr from the sample matrix using 2 N HCl. The Sr cuts were further purified using Eichrom Sr-spec resin based on the procedure from Andreasen and Sharma (2007). Briefly, the Sr cuts were loaded onto 100 μL columns in 5 N HNO_3. The sample matrix was removed from the column in 5 N HNO_3 and Sr was subsequently eluted in MQ H_2O. The Sr isotopic compositions of the mineral separates were measured on a Thermo Scientific® Triton *Plus* TIMS at the University of Münster. Approximately 1 μg of each sample or standard was loaded in 2 N HCl onto single Re filaments along with the Ta_2O_5 activator in phosphoric acid. Strontium isotopic measurements for the samples and standards were static runs consisting of 200 ratios using 16 s integration times, and each sample was measured two times on the same filament. Isobaric interferences from ^{87}Rb were monitored by simultaneously measuring ^{85}Rb with the Sr isotopes. Internal normalization was used to correct for mass bias effects using $^{86}Sr/^{88}Sr$ = 0.1194. Based on multiple analyses of the NBS 987 reference material, the 2SD for ε^{84}Sr was ±0.5 and the 2SD for $^{87}Sr/^{86}Sr$ was ±0.000013.

2.3.7 Uranium—Uranium purification was accomplished in the ICGL utilizing UTEVA resin following the procedure of Weyer et al. (2008). The $^{238}U/^{235}U$ composition of the samples was determined on the Thermo Scientific® Neptune MC-ICPMS at the ICGL following the ^{236}U-^{233}U double spike procedure discussed in Brennecka et al. (2010). Uncertainties on the $\delta^{238/235}$ U value of the Egg 2 mineral separates (reported as ±0.16) are calculated as the long-term reproducibility of standards run at the same concentrations (10-15 ppb U) as the samples.

3. RESULTS

3.1 Mass-dependent isotopic compositions

The mass-dependent isotopic compositions presented below are given in the most commonly used isotope ratios using the δ-notation: $\delta^{25/24}$Mg, $\delta^{44/40}$Ca, $\delta^{60/58}$Ni, $\delta^{56/54}$Fe, and $\delta^{238/235}$U (*e.g.*, Mullane et al., 2005; Brennecka et al., 2010; Wasserburg et al., 2012; Huang et al., 2012; Simon et al., 2017; Render et al., 2018).

3.1.1 Mg isotopic compositions—The $\delta^{25/24}$Mg of 11 Allende CAIs, bulk Allende, and BCR-2 are reported in Table 3 and Figure 2. The CAIs show considerable variation of $\delta^{25/24}$Mg ranging from −1.28 to +4.80, in agreement with literature data (*e.g.*, Niederer and Papanastassiou, 1984; Bizzarro et al., 2004; Thrane et al., 2006; Larsen et al., 2011;

Wasserburg et al., 2012). Furthermore, all fine-grained inclusions are characterized by light $\delta^{25/24}$Mg compositions, whereas the igneous CAIs show heavy $\delta^{25/24}$Mg signatures (Fig. 2).

3.1.2 Ca isotopic compositions—The Ca mass-dependent isotopic compositions of 11 Allende CAIs and the Egg 2 mineral separates relative to the NIST SRM915a reference material are presented in Figure 3 and Table 3. Most CAIs have light $\delta^{44/40}$Ca compositions in comparison to the bulk silicate earth (BSE) $\delta^{44/40}Ca_{BSE}$ = +1.05 (Huang et al., 2010), with values ranging from −8.28 to +0.60, and show good agreement with literature data (Niederer and Papanastassiou, 1984; Huang et al., 2012; Schiller et al., 2015; Simon et al., 2017; Bermingham et al., 2018). In contrast, CAI 173 has a heavy $\delta^{44/40}$Ca composition of +4.10. The Egg 2 mineral separates span a smaller range for $\delta^{44/40}$Ca of +0.02 to +0.40.

3.1.3 Ni isotopic compositions—The Egg 2 mineral separates have isotopically heavy and variable mass-dependent $\delta^{60/58}$Ni compositions spanning a range of +3.86 to +4.24 (Table 3). Also shown in Table 3 are the bulk CAI $\delta^{60/58}$Ni compositions from Render et al. (2018). Note that the Egg 2 samples show considerably heavier Ni isotopic compositions compared to all bulk CAI samples reported in Render et al. (2018). Furthermore, the Egg 2 separates give reasonably consistent results with the Egg 2 bulk measurement from Render et al. (2018).

3.1.4 Fe isotopic compositions—The mass-dependent Fe isotopic compositions of the CAIs and mineral separates are shown in Figure 4 and Table 4. The CAIs show variation in their $\delta^{56/54}$Fe ranging from −1.71 to +1.32, spanning a somewhat larger range than the literature data (Mullane et al., 2005; Hezel et al., 2008) (Fig. 4). Interestingly, all fine-grained CAIs exhibit light $\delta^{56/54}$Fe compositions whereas the igneous CAIs are characterized by both light and heavy $\delta^{56/54}$Fe compositions. The $\delta^{56/54}$Fe values in the Egg 2 mineral separates (~ +4.3 to +9.6) span a range that is both considerably larger and isotopically heavier than the bulk CAIs or any other meteoritic or terrestrial material yet reported. The terrestrial rock standards and bulk Allende measured in this study have $\delta^{56/54}$Fe compositions that are indistinguishable within the analytical uncertainties and are in good agreement with literature data (*e.g.,* Dauphas et al., 2004; Weyer et al., 2005; Craddock and Dauphas, 2011; Schuth et al., 2015). The $\delta^{56/54}$Fe values for the Egg 2 mineral separates and A-ZH-1 are corrected for nucleosynthetic isotopic compositions using their respective $\varepsilon^{56}Fe_{corr.}$ (see electronic annex). However, the correction for nucleosynthetic anomalies are significantly smaller than the degree of mass-dependent fractionation (*e.g.*, Egg 2 high-Fe Px $\delta^{56/54}Fe_{measured}$ = +9.85; $\delta^{56/54}Fe_{corr.}$ = +9.66).

3.2 Nucleosynthetic Fe isotopic compositions

The nucleosynthetic Fe isotopic compositions of the samples and standards are presented in Figure 5 and Table 4. The terrestrial rock standards and bulk Allende are indistinguishable from the bracketing standard solution and are in good agreement with literature data (*e.g.*, Völkening and Papanastassiou, 1989; Weyer et al., 2005; Dauphas et al., 2004; Tang and Dauphas, 2012). The bulk CAIs do not show any resolvable ε^{56}Fe variations. However, the Egg 2 mineral separates have resolvable excesses in ε^{56}Fe that span a range from +0.97 to +2.38 (Table 4). Given the highly fractionated Fe in the Egg 2 mineral separates ($\varepsilon^{56/54}$Fe ~

+4.3 to +9.6), it is plausible that the use of the exponential law for mass bias correction is not accurate, resulting in mass-independent effects such as an artificial anomaly on ε^{56}Fe (similar to that discussed for Ni in Render et al., 2018). As such, following Render et al. (2018) a second-order mass fractionation correction was applied to all samples. The specific details of this second-order correction follow calculations performed by Tang and Dauphas, (2012) and are provided in the electronic annex. For most samples, the correction does not change the ε^{56}Fe or ε^{58}Fe values outside the analytical uncertainties. However, this correction results in lower ε^{56}Fe values for the Egg 2 mineral separates (*e.g.*, Egg 2 high Fe-px $\varepsilon^{56}Fe_{meas.} = 2.34$, $\varepsilon^{56}Fe_{corr.} = 1.88$) which are still well-resolved from the terrestrial composition (Fig. 5a). In contrast, none of the investigated samples display resolvable ε^{58}Fe variations (Fig. 5b).

3.3 Comparison of Egg 2 mineral separates with bulk Egg 2

Figure 6 shows a comparison of our mass-dependent and mass-independent Fe isotope data for the Egg 2 mineral separates with that for bulk Egg 2 reported by Völkening and Papanastassiou, (1989). Note that the mass-independent data for the Egg 2 mineral separates also have a second-order mass fractionation correction using the same procedure described in section 3.2. Figure 6 demonstrates that the isotopic fractionation (F) and ε^{57}Fe in Egg 2 mineral separates are consistent with the data for bulk Egg 2 (Fig. 6a/b). However, the Egg 2 mineral separates do not exhibit the previously reported excess of ~28 on ε^{58}Fe (Fig. 6c). The reason for this discrepancy in the ε^{58}Fe values between the bulk Egg 2 CAI and the mineral separates is currently unknown. However, Chen et al. (2014) reported a ε^{64}Ni excess (of ~32) in Egg 2, which was also not reproduced by an Egg 2 Ni measurement by Render et al. (2018). In fact, Render et al. (2018) observed a much smaller excess of ~2 ε-units in ^{64}Ni. As Render et al. (2018) and this work, which have both investigated the same Egg 2 mineral separates, have not reproduced previously reported values for the bulk Egg 2 sample, it is unclear if this is related to sample heterogeneity (unlikely for an igneous CAI) or if it reflects an analytical difference.

3.4 Ti, Ni, Sr, and U isotopic compositions of the Egg 2 mineral separates

The Ti, Ni, Sr, and U isotopic compositions of the Egg 2 mineral separates are presented in Table 3 (U) and Table 5 (Ti, Ni, Sr). All separates display resolved excesses in ε^{46}Ti and ε^{50}Ti, consistent with literature CAI data (*e.g.*, Williams et al., 2016; Davis et al., 2018; Ebert et al., 2018). Because of low Ni contents, no nucleosynthetic Ni isotopic compositions are available for Egg 2 Plag or Egg 2 high-Mg Px. The Egg 2 high-Fe Px separate shows resolvable excesses in ε^{60}Ni, ε^{62}Ni, and ε^{64}Ni, which are slightly larger than the values reported for a bulk sample of this CAI (Render et al., 2018) (Table 5). Specifically, the Egg 2 bulk has ε^{60}Ni, ε^{62}Ni, and ε^{64}Ni of 0.71, 1.07, and 1.75, respectively, while Egg 2 high-Fe Px has ε^{60}Ni, ε^{62}Ni, and ε^{64}Ni of 0.78, 1.33, and 2.25, respectively. Relative to terrestrial standards, the mineral separates have ε^{84}Sr values spanning a range of +1.2 to +1.6. These values agree within analytical uncertainty with each other and with bulk CAI Sr data (Moynier et al., 2012; Hans et al., 2013; Paton et al., 2013; Brennecka et al., 2013; Shollenberger et al., 2018; Myojo et al., 2018). Lastly, the $\delta^{238/235}$U compositions of the mineral separates are indistinguishable from one another within analytical uncertainty and

are consistent with literature data from igneous CAIs (Brennecka et al., 2010; Amelin et al., 2010; Connelly et al., 2012; Tissot et al., 2016).

4. DISCUSSION

Given the refractory nature of CAIs and their constituents, elements with moderately volatile behavior, such as Fe, are not expected to be abundant in CAIs. The predicted low abundance of indigenous Fe in CAIs means that secondary Fe, particularly when Fe is found at the wt% level, can effectively overprint any original isotopic signature that was present in the CAI. Previous literature has reported that Fe in meteoritic components such as CAIs and chondrules (*e.g.*, Mullane et al., 2005) is highly susceptible to nebular and/or parent body alteration. Therefore, before assigning a meaning to the measured Fe isotopic variations in our CAIs, we here use the Mg, Ca, and U mass-dependent isotope fractionations of individual CAIs in combination with their respective REE patterns to assess their formation history and any subsequent processing or potential alteration. The combination of mass-dependent isotope signatures along with REE patterns can help us to understand the condensation and evaporation events experienced by these CAIs.

4.1 The relationship between $\delta^{25/24}$Mg, $\delta^{44/40}$Ca, petrologic type, and REE pattern in CAIs

The Mg isotopic compositions of our CAIs show stark differences between fine-grained and igneous inclusions (Fig. 7). In particular, fine-grained CAIs, which have not undergone melting, are characterized by light Mg isotope compositions ($\delta^{25/24}$Mg values range between −0.5 and −1.3). In comparison, igneous CAIs, which were thermally processed, display heavy $\delta^{25/24}$Mg signatures (ranging between +3.0 and +4.8). For mass-dependent Ca isotopic compositions, most CAIs of this work have isotopically light $\delta^{44/40}$Ca compositions relative to the BSE (Fig. 7), regardless of their petrologic classification. Our samples are consistent with previous literature data, yet span a larger range ($\delta^{44/40}$Ca: −8.28 to +4.10), including one CAI with a heavy $\delta^{44/40}$Ca signature (CAI 173 , $\delta^{44/40}$Ca = +4.10). This particular CAI is a fine-grained/altered Type A inclusion with a group III REE pattern and contains significant amounts of secondary minerals such as sodalite and nepheline (Brennecka et al., 2017a), all of which exemplify its complex history and could potentially explain its heavy $\delta^{44/40}$Ca signature.

In addition to being related to their petrologic type, the $\delta^{25/24}$Mg compositions of the CAIs are also consistent with their REE patterns, as all group II CAIs have light $\delta^{25/24}$Mg compositions whereas all group I CAIs are characterized by heavy $\delta^{25/24}$Mg compositions (Fig. 7). The CAIs with group II REE patterns are believed to have formed from a gas from which an ultra-refractory component had previously been removed; therefore, this pattern indicates gas/solid separation during incomplete evaporation or fractional condensation (Boynton, 1975; Davis and Grossman, 1979). Interestingly, the group III CAIs have variable $\delta^{25/24}$Mg values ranging from −0.5 to +4.1, depending on whether they are fine-grained or igneous. The group III REE pattern is relatively unfractionated except for negative anomalies in Eu and Yb, both of which are more volatile than the other REE. Similarly, and in agreement with previous observations (Huang et al., 2012; Simon et al., 2017; Bermingham et al., 2018), the $\delta^{44/40}$Ca signatures of our CAIs are also related to their REE

patterns (Fig. 7). For example, CAIs with lighter $\delta^{44/40}$Ca signatures ranging from −8.28 to −1.40 have group II REE patterns. In comparison, CAIs with heavier $\delta^{44/40}$Ca of −0.68 to +0.60 (*i.e.*, close to the BSE value of $\delta^{44/40}$Ca = +1.05) have group I REE patterns. However, unlike previous Ca isotope work on CAIs, we also see that CAIs with group III patterns have variable $\delta^{44/40}$Ca ranging from −4.70 to +4.10 (CAI 165, CAI 171, CAI 173), again depending on whether they are fine-grained or igneous inclusions. In contrast to the bulk CAIs, the mineral separates from Egg 2 span a small range for $\delta^{44/40}$Ca of +0.02 to +0.40, which is within the values previously reported for inter-mineral fractionation in silicates (*e.g.*, Huang et al., 2010; Ryu et al., 2011; Feng et al., 2014; Schiller et al., 2016). In summary, isotopic differences in $\delta^{25/24}$Mg and $\delta^{44/40}$Ca are observed for all CAIs of this work, and these appear to be related to their REE patterns and their petrologic type (*i.e.*, fine-grained or igneous). Therefore, combining the mass-dependent Mg and Ca signatures may provide insight into the formation histories of the various inclusions.

The mass-dependent Mg and Ca isotopic compositions are plotted together in Figure 7. The lack of a linear correlation between the Mg and Ca isotopic compositions probably reflects the differing condensation temperatures of the elements. Calcium has a 50% T_c of ~ 1520K, whereas Mg has a 50% T_c of ~ 1340K (Lodders, 2003). As the difference between these temperatures is ~ 180K, this may play a role in the observed isotopic differences. For example, at a temperature of ~ 1520K about half of the Ca is expected to condense, whereas very little, if any, Mg would have condensed, resulting in very different Ca and Mg isotopic behavior in the condensate. However, regardless of the lack of a linear correlation between the two elements for all samples, the clear distinction between fine-grained CAIs and igneous CAIs (Fig. 7) suggests that each of these two types underwent distinct formation histories.

The cause of the Mg and Ca isotopic variations among these CAIs is most likely related to multiple high-temperature condensation and/or evaporation processes in the solar nebula. This has previously been reported for elements such as Si and Ti along with Mg and Ca (Niederer and Papanastassiou, 1984; Davis et al., 2018; and references therein). For example, all CAIs with group II REE patterns have isotopically light $\delta^{25/24}$Mg and $\delta^{44/40}$Ca values, consistent with kinetic isotope fractionation during condensation. In comparison, CAIs that do not lack the ultra-refractory component exhibit near-chondritic $\delta^{44/40}$Ca values (chondrites span a range of $\delta^{44/40}$Ca from +0.10 to +1.54; Bermingham et al., 2018), heavier $\delta^{25/24}$Mg compositions relative to group II CAIs, and flat REE patterns. On the other hand, CAIs with group III REE patterns span wider ranges in both $\delta^{44/40}$Ca and $\delta^{25/24}$Mg. The isotope compositions of these CAIs likely reflect that these samples or their precursor materials experienced multiple thermal events (causing isotopic variability) under changing redox conditions (as these group III CAIs have depletions in the redox sensitive Eu and Yb; *e.g.,* Ruzicka et al., 2012). Overall, the light $\delta^{44/40}$Ca signatures of most CAIs probably reflect the isotopic compositions of early formed precursor condensates that were enriched in the lighter isotopes, regardless of inclusion type and subsequent history (which for igneous CAIs involved re-melting). For Mg, the fine-grained CAIs have light $\delta^{25/24}$Mg compositions representative of an early condensate, and igneous inclusions have heavy $\delta^{25/24}$Mg compositions that are dominated by evaporative processes. Taken together, this suggests that temperatures during melting of the igneous inclusions were high enough to

result in significant Mg evaporation and little, if any, Ca evaporation. Therefore, the combined $\delta^{25/24}$Mg, $\delta^{44/40}$Ca, and REE patterns demonstrate multiple stages of condensation and evaporation in these CAIs.

4.2 On the origin of U isotopic variation in the early Solar System

Understanding U isotope fractionation in CAIs is important because the $^{238}U/^{235}U$ isotope ratio is used in calculating the absolute ages of these objects, which are used to define the age of the Solar System. It has previously been suggested that—along with the decay of ^{247}Cm to ^{235}U ($t_{1/2}$ = 15.6 Ma)—isotopic fractionation during CAI-forming processes may have contributed to U isotope variation in CAIs (Brennecka et al., 2010; Tissot et al., 2016). As the $\delta^{25/24}$Mg measured in our CAIs is indicative of isotope fractionation during evaporation and/or condensation processes and U isotopes can be fractionated during such processes, examining $\delta^{25/24}$Mg and U isotope compositions in the same samples may aid in understanding the causes for U isotope variations in CAIs. As seen in Fig. 8, igneous CAIs show a linear correlation between $\delta^{25/24}$Mg and $\delta^{238/235}$U (with a correlation coefficient of 0.74). Furthermore, these igneous CAIs plot along a line that has a slope consistent with a theoretical Rayleigh fractionation line (Fig. 8). This relationship suggests that isotopic fractionation during thermal processing of the igneous CAIs contributed to the relatively small U isotope variation in this subset of samples. Such an observation would be consistent with our interpretation that igneous CAIs experienced evaporation events that drove the $\delta^{25/24}$Mg (and $\delta^{238/235}$U) signatures to heavier values. However, compared to igneous CAIs the fine-grained CAIs show a much larger range of U isotopic compositions that do not correlate with $\delta^{25/24}$Mg, suggesting that isotope fractionation during evaporation/condensation processes alone cannot explain the range of data by itself. Additionally, U isotopic compositions in these fine-grained samples correlate with proxies for initial Cm concentration (*i.e.*, Th and Nd concentrations, Brennecka et al., 2010; Tissot et al., 2016). Therefore, the large-scale (>1‰) $\delta^{238/235}$U isotopic variation in fine-grained inclusions is likely due to the decay of the short-lived radionuclide ^{247}Cm in the early Solar System, consistent with previous findings in this and other sample sets (Brennecka et al., 2010; Tissot et al., 2016).

4.3 Fe isotopic variations in CAIs and Egg 2 mineral separates

4.3.1 Mass-dependent $\delta^{56/54}$Fe signatures of bulk CAIs and Egg 2 mineral separates—

The CAIs of this work have variable mass-dependent $\delta^{56/54}$Fe signatures, similar to what has been reported for other elements like Ca, Ti, and Ni in CAIs (*e.g.*, Huang et al., 2012; Simon et al., 2017; Davis et al., 2018; Bermingham et al., 2018; Render et al., 2018). Although most of our data are in good agreement with previous work on Fe isotopic fractionation in CAIs (Mullane et al., 2005; Hezel et al., 2008), our CAI sample set spans a wider range of $\delta^{56/54}$Fe (−1.71 to +1.29‰). Furthermore, most of our CAIs are isotopically distinct from bulk Allende ($\varepsilon^{56/54}$Fe = −0.03 ± 0.08). As CAIs almost certainly contain a portion of secondary Fe (*i.e.*, Fe not indigenous to the CAIs), variations in $\delta^{56/54}$Fe could, to variable extents, also reflect secondary contamination which may increase or decrease $\delta^{56/54}$Fe variations, thus making the interpretation of the $\delta^{56/54}$Fe signatures more difficult.

The Egg 2 mineral separates may provide an alternative pathway to investigate the Fe isotopic composition of CAIs. Unlike some CAIs that have been reported to have FeO contents >7 wt.% (Mullane et al., 2005), the bulk Egg 2 inclusion has a FeO content of 0.69% (Wark and Lovering, 1982), demonstrating that it has not experienced severe secondary contamination. In comparison to bulk CAIs of this study, the Egg 2 mineral separates have extremely heavy $\delta^{56/54}$Fe compositions (ranging from +4.3 to +9.7). Previous work reported inter-mineral differences between terrestrial olivine and clinopyroxene of up to 0.2‰ (*e.g.*, Beard et al., 2004; Liu et al., 2014), thus demonstrating that whereas $\delta^{56/54}$Fe signatures can vary between mineral phases, the differences are relatively small compared to the fractionation seen in the Egg 2 mineral separates. This is in stark contrast to the small range of $\delta^{44/40}$Ca signatures (+0.02 to +0.40) of the Egg 2 mineral separates that are explained by inter-mineral fractionation. Therefore, the range of $\delta^{56/54}$Fe in the Egg 2 mineral separates requires an alternative explanation.

Different processes that could induce Fe isotope fractionation resulting in variable $\delta^{56/54}$Fe signatures include diffusion and evaporation/condensation events. Diffusion, a secondary process, could potentially be responsible for the $\delta^{56/54}$Fe variations illustrated in Fig. 4, although this seems rather unlikely. In the case of the Egg 2 mineral separates, diffusion alone is unlikely to generate ~6‰ of $\delta^{56/54}$Fe variation, as the effect on Fe isotopes in magmatic minerals due to this process barely exceeds ~1‰ (Sio et al., 2013; Oeser et al., 2015). Moreover, because the range of $\delta^{56/54}$Fe in CAIs is much larger than that in bulk meteorites ($\delta^{56/54}$Fe ~ 0; *e.g.*, Craddock and Dauphas, 2011), parent body alteration alone cannot easily account for it. Thus, given the range of $\delta^{56/54}$Fe in CAIs and the Egg 2 mineral separates (Fig. 4), an additional mode of fractionation is required to fully explain these isotopic signatures.

Contrary to diffusion, evaporation and condensation events can generate large isotopic variability and could be primary contributors to the isotopic signatures of CAIs. For example, CAIs with light $\delta^{56/54}$Fe signatures could reflect the kinetic condensation of Fe, as this process favors the light isotopes. Another scenario could be that the heavy $\delta^{56/54}$Fe signatures of the Egg 2 separates and other CAIs reflects crystallization from a melt that was unfractionated when it formed or even slightly heavy ab initio. This would be followed by possibly re-melting and extensive evaporation of Fe (probably occurring in multiple events), driving the $\delta^{56/54}$Fe compositions to progressively heavier values. The change in $\delta^{56/54}$Fe through partial evaporation of Fe can be modeled using a simple single-stage Rayleigh distillation model to describe the observed $\delta^{56/54}$Fe signatures of the CAIs and Egg 2 mineral separates. For most of the bulk CAIs, this requires less than 15% of the Fe to be evaporated, similar to implications based on the isotope compositions of elements like Ti and Ni (Davis et al., 2018; Render et al., 2018), to arrive at the measured compositions. In comparison, the Fe isotope compositions of the Egg 2 mineral separates would require evaporation of ~30 to 50% of the Fe as the melt crystallized. Although these represent only rough estimations because the starting composition is not well-defined (we use the lightest CAI for our starting composition). Finally, one might be able to determine whether other processes like mixing played a role in determining the $\delta^{56/54}$Fe signatures by examining the Fe nucleosynthetic variations in the Egg 2 mineral separates.

4.3.2 Nucleosynthetic variations—None of the bulk CAIs of this work display resolved ε^{56}Fe or ε^{58}Fe nucleosynthetic anomalies (Fig. 5). On the other hand, the Egg 2 mineral separates all have resolved excesses in ε^{56}Fe relative to terrestrial standards and bulk Allende. Therefore, given that the sum of the Egg 2 mineral separates would not be 0 for ε^{56}Fe, this is in stark contrast to the bulk CAIs of this work. As the bulk CAIs do not have any excesses in ε^{56}Fe, it is important to understand whether the Egg 2 inclusion is unique or whether it is representative of the CAI-forming region. Previous work on the Egg 2 inclusion hinted at excesses in ε^{56}Fe, but this was not resolved from the terrestrial composition (data renormalized from Völkening and Papanastassiou, 1989). Alternatively, it is also possible that certain non-magnetic Fe-rich phases with ε^{56}Fe of <0 could have been lost during the mineral separation process. Regardless, the Egg 2 mineral separates have nucleosynthetic Ti, Ni, and Sr isotope anomalies indistinguishable from other bulk CAIs (see section 3.4). Therefore, we have confidence that the Egg 2 separates are broadly representative of the CAI-forming region. Interestingly, the mineral separate with the highest magnetic susceptibility (high-Fe Px) displays the largest excess in ε^{56}Fe, while the non-magnetic separate (plagioclase) has the smallest anomaly (Fig. 5a). This suggests that the magnetic high-Fe Px held onto its original signature, as it is possibly more resistant to alteration or more difficult to overprint due to the higher amount of original Fe in that phase compared to the plagioclase phase. Therefore, the Egg 2 mineral separates may assist in locating the primary Fe of the CAI, as phases such as high-Fe Px could host more indigenous Fe.

Interestingly, when the ε^{56}Fe (nucleosynthetic) values are plotted against $\delta^{56/54}$Fe (mass-dependent) values in bulk CAIs and Egg 2 mineral separates, a linear correlation is observed (Fig. 9; please see electronic annex for concerns about an analytical artifact). Whereas such a correlation could, in principle, represent severe mass-dependent fractionation causing apparent mass-independent effects, these samples have a second-order correction applied for natural mass fractionation (following a Rayleigh distillation; Tang and Dauphas, 2012) as recently demonstrated by Render et al. (2018). It is possible that the mass fractionation law(s) for correction of large $\delta^{56/54}$Fe are poorly known, resulting in a false correction. However, another explanation is that high-Fe pyroxene, the separated phase least susceptible to alteration, also contains the most original (*i.e.*, indigenous) Fe, while Fe from secondary processes is incorporated into less magnetic (and less Fe-rich) phases such as the plagioclase fraction. Therefore, we interpret the coupling of mass-dependent and nucleosynthetic anomalies of Fe isotopes to indicate that the indigenous Fe isotope composition of the CAIs that has been highly fractionated by evaporation processes mixed with that of less fractionated and less isotopically anomalous Fe that was condensed while still in the nebula. In such a scenario, the high-Fe pyroxene separate represents the most pristine Fe isotopic composition, as it contained the highest percentage of original Fe from CAI formation. The Mg-rich pyroxene, and more so the plagioclase separate, would be more affected by subsequent contamination and, therefore, contain progressively more secondary Fe. Such a relationship between mass-dependent and nucleosynthetic isotopic compositions in CAIs has been reported for Ni (Render et al., 2018), likely indicating that both types of isotopic variations for each individual element have a common origin.

4.4 Ti, Ni, Sr, and U isotopic compositions in Egg 2 mineral separates

As the Egg 2 mineral separates display variable Fe isotopic compositions, their Ti, Ni, Sr, and U isotopic compositions were also measured in order to better understand the cause of their ε^{56}Fe variations. While the mineral separates display isotopic variations in Ti, Ni, Sr, and U that are in agreement with literature data (*e.g.*, Brennecka et al., 2010, 2013; Williams et al., 2016; Davis et al., 2018; Render et al., 2018), they are not correlated with the ε^{56}Fe variations reported here (Fig. 10a/b). For example, all three mineral separates have ε^{50}Ti ≈ +9, ε^{84}Sr ≈ +1.2, and $\delta^{238/235}$U ≈ −0.35, which are consistent with the majority of bulk igneous CAIs. Thus, the δ^{50}Ti, δ^{84}Sr, and $\delta^{238/235}$U compositions reflect that the anomalous carriers of these elements were homogenized and the isotope anomalies equilibrated between the different mineral phases, probably during melting and subsequent crystallization of this igneous inclusion.

4.5 Location of mixing and secondary alteration in CAIs

The correlation between $\delta^{56/54}$Fe and ε^{56}Fe signatures in bulk CAIs and Egg 2 mineral separates likely indicates the mixing of original Fe in CAIs with Fe from later formed Fe-bearing phases. In this scenario, the original CAI component would have higher $\delta^{56/54}$Fe and ε^{56}Fe values than the later formed Fe component, which would have values similar to that of bulk Allende. As such, the two most likely places for mixing to occur are 1) in the nebula or 2) on the parent body. The effects of Fe-alkali-halogen metasomatism, the likely source of Fe contamination in CAIs, have been well-documented, but it is debated whether this occurred in the nebula or on the asteroidal body (*e.g.*, Krot et al., 1995). By examining Al-Mg isotope systematics in secondary minerals of Allende CAIs, Fagan et al. (2007) demonstrated that the possible timing of secondary alteration ranged from when CAIs started forming up to a time after CAIs were incorporated on their asteroidal bodies. As such, the Al-Mg systematics demonstrate that secondary alteration could have occurred either in the nebula and/or on the parent body. However, Fe isotopic compositions of bulk CAIs and Egg 2 mineral separates may provide evidence as to where the Fe alteration/mixing most likely occurred.

Fine-grained CAIs, which have no petrological evidence for melting after they condensed, have the lightest $\delta^{56/54}$Fe compositions, which may reflect the condensation of isotopically light “primary” Fe from the CAI-forming region and a lack of subsequent Fe evaporation. However, four of these fine-grained CAIs (166, 167, 173, 175) show significant amounts of secondary mineralization, ranging from ~18% to 42% (Brennecka et al., 2017a), and lack a strong correlation between $\delta^{56/54}$Fe and percentage of secondary minerals. If the secondary minerals were incorporated on the Allende parent body where the $\delta^{56/54}$Fe signature is well known ($\delta^{56/54}Fe = -0.007‰$ Craddock and Dauphas, 2011), then secondary Fe would have a similar $\delta^{56/54}$Fe signature to bulk Allende. Demonstratively, this is not the case, as all fine-grained CAIs of this work have light $\delta^{56/54}$Fe signatures (Fig. 4). Therefore, secondary alteration must have occurred prior to the parent body phase and this likely occurred in the nebula while Fe-bearing phases were condensing.

In contrast, igneous CAIs, which show far lower percentages of secondary minerals compared to fine-grained CAIs, exhibit a range of $\delta^{56/54}$Fe compositions. As previously

shown for chondrules, molten extraterrestrial materials exhibit isotopically heavy $\delta^{56/54}$Fe compositions, most likely reflecting heating events (and associated evaporation) that drove off the light Fe isotopes (Mullane et al., 2005). Since igneous CAIs were once molten droplets, the heavy Fe isotope signatures recorded by some of these CAIs are probably manifestations of such heating events, consistent with their isotopically heavy Mg compositions (Fig. 11). However, a large portion of the igneous CAIs reported here have light Fe isotopic signatures. This could suggest that 1) these CAIs (or their precursors) started with isotopically light Fe compositions and experienced less extensive evaporation-induced fractionation than other igneous samples or 2) isotopically light Fe was added to igneous CAIs in the nebula from metasomatism. Similar to fine-grained CAIs, the light isotope signatures recorded by igneous CAIs must have been acquired during condensation.

4.6 Probing the original Fe isotopic composition of the CAI-forming region

The lack of Fe isotopic anomalies in our bulk CAIs likely reflects the mixing of secondary Fe into CAIs that heavily diluted any nucleosynthetic anomaly towards the bulk meteorite or terrestrial value. As such, the mass-independent Fe isotope compositions reported here are secondary and do not represent the original Fe in the CAIs, but they rather reflect the Fe isotope composition at the time of secondary alteration in the nebula. However, the Egg 2 mineral separates offer an alternative approach to probe the original mass-independent Fe isotopic composition of the CAI-forming region. The Egg 2 mineral separates have Ti, Ni, and Sr nucleosynthetic anomalies indistinguishable from CV, CK, and CO CAIs (*e.g.*, Moynier et al., 2012; Brennecka et al., 2013; Hans et al., 2013; Paton et al., 2013; Williams et al., 2016; Davis et al., 2018; Render et al. 2018; Myojo et al., 2018), suggesting that they are derived from the same isotopic reservoir as most other “normal” CAIs. Therefore, the Fe isotopic compositions of the Egg 2 mineral separates may be a good proxy for understanding what the original Fe isotopic composition of the CAI-forming region was.

Our data suggest that the CAI-forming region had an excess in ^{56}Fe (likely a minimum of ~2ε) and no resolved difference in ^{58}Fe, recorded by the most pristine mineral separate. As other Fe-group elements typically display excesses in their most neutron-rich isotopes (*e.g.*, ^{48}Ca, ^{50}Ti, ^{64}Ni), this has important implications for the sources of material in early Solar System reservoirs. Wasserburg et al. (2015) predicted excesses in ^{58}Fe and ^{64}Ni from the *s*-process in AGB stars, but what is observed for the Egg 2 mineral separates are excesses in ^{56}Fe, and to a much lesser extent excesses in ^{64}Ni compared to the model. Nittler et al. (2003) stated that Type Ia supernovae are believed to be the primary sources of ^{56}Fe, and, therefore, the excess ^{56}Fe in CAIs may be a signature of such material incorporated in the CAI-forming region. Type Ia supernovae are thought to also produce the neutron-rich isotopes ^{62}Ni, ^{64}Ni, ^{54}Cr, and ^{50}Ti (*e.g.*, Hartmann et al., 1985), which are enriched in most CAIs. Taken together, this may suggest that the isotopic composition of the CAI-forming region may have a larger percentage of supernovae-derived material, possibly from Type Ia supernovae, than previously thought. Such an observation is important for understanding stellar evolution and the types of stars that contributed material to the CAI-forming region and subsequent regions of the protoplanetary disk.

5. Conclusions

1) For Mg, Ca, and Fe mass-dependent isotopic compositions, fine-grained CAIs are in general isotopically lighter than igneous CAIs. This most likely reflects the fact that igneous CAIs experienced more significant evaporation, as these CAIs were once molten, driving their isotopic compositions toward heavier values. Furthermore, the mass-dependent Mg, Ca, and Fe isotope compositions of both types of CAIs are consistent with expectations from their REE patterns.

2) As evidenced by their mass-dependent Fe isotope compositions, the secondary alteration that added Fe to CAIs must have happened in the nebula and not on the parent body. Otherwise, CAIs studied here would have had $\delta^{56/54}$Fe signatures similar to bulk Allende, which they demonstrably do not. Instead, CAIs retain predominantly isotopically light $\delta^{56/54}$Fe signatures (relative to bulk chondrites) that are due to secondary condensation of Fe in the nebula.

3) None of our bulk CAIs exhibit resolvable nucleosynthetic Fe isotope anomalies. However, three mineral separates of the Allende Egg 2 CAI show that the original Fe isotopic composition of the CAI-forming region was enriched in ^{56}Fe. At the current level of precision, we did not resolve any mass-independent anomalies in ^{58}Fe for the three mineral separates.

Supplementary Material

Refer to Web version on PubMed Central for supplementary material.

Acknowledgments

This work was supported by a Sofja Kovalevskaja award from the Alexander von Humboldt Foundation (G.A.B.) and a NASA Emerging Worlds award (NNX15AH41G to M.W.). We thank C. Burkhardt for assistance with Ti isotopic measurements and for providing samples, T. Kruijer for providing CAI samples, T. Kleine for fruitful discussions, and the late G.J. Wasserburg for providing the Egg 2 sample. The authors thank Dimitri Papanastassiou and two anonymous reviewers for their helpful comments that improved the manuscript.

References

Amelin Y, Kaltenbach A, Iizuka T, Stirling CH, Ireland TR, Petaev M, and Jacobsen SB (2010) U-Pb chronology of the Solar System's oldest solids with variable ^{238}U/^{235}U. Earth Planet. Sci. Lett 300, 343–350.

Amsellem E, Moynier F, Pringle EA, Bouvier A, Chen H, and Day JMD (2017) Testing the chondrule-rich accretion model for planetary embryos using calcium isotopes. Earth Planet. Sci. Lett 469, 75–83.

Andreasen R and Sharma M (2007) Mixing and Homogenization in the early solar system: clues from Sr, Ba, Nd, and Sm Isotopes in Meteorites. Astrophys. J 665, 874–883.

Arnold GL, Weyer S, and Anbar AD (2004) Fe isotope variations in natural materials measured using high mass resolution multiple collector ICPMS. Anal. Chem 76, 322–327. [PubMed: 14719878]

Beard BL and Johnson CM (2004) Inter-mineral Fe isotope variations in mantle-derived rocks and implications for the Fe geochemical cycle. Geochim. Cosmochim. Acta 68, 4727–4743.

Berglund M and Wieser ME (2011) Isotopic compositions of the elements 2009 (IUPAC Technical Report) Pure Appl. Chem 83, 397–410.

Bermingham KR, Gussone N, Mezger K, and Krause J (2018) Origins of mass-dependent and mass-independent Ca isotope variations in meteoritic components and meteorites. Geochim. Cosmochim. Acta 226, 206–223.

Birck JL and Allègre CJ (1984) Chromium isotopic anomalies in Allende refractory inclusions. Geophys Res Lett. 11, 943–946.

Birck JL and Allègre CJ (1985) Evidence for the presence of 53Mn in the early solar system. Geophys Res Lett. 12, 745–748.

Birck JL and Lugmair GW (1988) Nickel and chromium isotopes in Allende inclusions. Earth Planet. Sci. Lett 90, 131–143.

Bischoff A and Keil K (1984) Al-rich objects in ordinary chondrites: Related origin of carbonaceous and ordinary chondrites and their constituents. Geochim. Cosmochim. Acta 48, 693–709.

Bizzarro M, Baker JA, and Haack H (2004) Mg isotope evidence for contemporaneous formation of chondrules and refractory inclusions. Nature 431, 275–278. [PubMed: 15372023]

Boynton WV (1975) Fractionation in the solar nebula: condensation of yttrium and the rare earth elements. Geochim. Cosmochim. Acta 39, 569–584.

Bouvier A, Brennecka GA, and Wadhwa M (2011a) Absolute chronology of the first solids in the solar system. Workshop on Formation of the First Solids in the Solar System, #9054.

Bouvier A, Spivak-Birndorf LJ, Brennecka GA, and Wadhwa M (2011b) New constraints on early Solar System chronology from Al–Mg and U–Pb isotope systematics in the unique basaltic achondrite Northwest Africa 2976. Geochim. Cosmochim. Acta 75, 5310–5323.

Brennecka GA, Weyer S, Wadhwa M, Janney PE, Zipfel J, and Anbar AD (2010) $^{238}U/^{235}U$ Variations in Meteorites: Extant ^{247}Cm and Implications for Pb-Pb Dating. Science 327, 449–451. [PubMed: 20044543]

Brennecka GA, Borg LE, and Wadhwa M (2013) Evidence for supernova injection into the solar nebula and the decoupling or r-process nucleosynthesis. Proc. Nat. Acad. Sci 110, 17241–17246. [PubMed: 24101483]

Brennecka GA, Borg LE, Romaniello SJ, Souders AK, Shollenberger QR, Marks NE, and Wadhwa M (2017a) A renewed search for short-lived ^{126}Sn in the early Solar System: Hydride generation MC-ICPMS for high sensitivity Te isotopic analysis. Geochim. Cosmochim. Acta 201, 331–344.

Brennecka GA, Burkhardt C, Kruijer TS, and Kleine T (2017b) Towards understanding the source of nucleosynthetic anomalies in refractory inclusions Lunar Planet. Sci. XLVIII Lunar Planet. Inst, Houston. #1619 (abstr.).

Burkhardt C, Kleine T, Bourdon B, Palme H, Zipfel J, Friedrich JM, and Ebel DS (2008) Hf-W mineral isochron for Ca,Al-rich inclusions: Age of the solar system and the timing of core formation in planetesimals. Geochim. Cosmochim. Acta 72, 6177–6197.

Burkhardt C, Kleine T, Oberli F, Pack A, Bourdon B, and Wieler R (2011) Molybdenum isotope anomalies in meteorites: constraints on solar nebula evolution and origin of the Earth. Earth Planet. Sci. Lett 312, 390–400.

Burkhardt C (2012) Molybdenum isotopes and solar nebula evolution Ph.D. dissertation, ETH Zurich, Zurich.

Burkhardt C, Borg LE, Brennecka GA, Shollenberger QR, Dauphas N, and Kleine T (2016) A nucleosynthetic origin for the Earth's anomalous ^{142}Nd composition. Nature 537, 394–398. [PubMed: 27629643]

Carlson RW, Boyet M, and Horan M (2007) Chondrite barium, neodymium, and samarium isotopic heterogeneity and early Earth differentiation. Science 316, 1175–1178. [PubMed: 17525335]

Chen H-W, Lee T, Lee D-C, and Iizuka Y (2009) In situ Ti isotopic measurements by laser ablation MC-ICP-MS. Terr. Atmos. Ocean. Sci 20, 703–712.

Chen JH and Papanastassiou DA (2014) Endemic 64Ni effects in Allende Ca-Al-Rich inclusions Lunar Planet. Sci. XLV Lunar Planet. Inst, Houston. #2327 (abstr.).

Clayton RN and Mayeda TK (1977) Correlated oxygen and magnesium isotope anomalies in Allende inclusions. I. Oxygen Geophys. Res. Letters 4, 295–298.

Connelly JN, Bizzarro M, Krot AN, Nordlund Å, Wielandt D, and Ivanova MA (2012) The absolute chronology and thermal processing of solids in the solar protoplanetary disk. Science 338, 651–655. [PubMed: 23118187]

Cook DL and Schönbächler M (2017) Iron isotopic compositions of troilite (FeS) inclusions from iron meteorites. Astron. J 154, 172–179.

Craddock PR and Dauphas N (2011) Iron isotopic compositions of geological reference materials and chondrites. Geostand. Geoanalytical Res 35, 101–123.

Dauphas N and Schauble EA (2016) Mass fractionation laws, mass-independent effects, and isotopic anomalies. Annu. Rev. Earth Planet. Sci 44, 709–783.

Dauphas N, Janney PE, Mendybaev RA, Wadhwa M, Richter FM, Davis AM, van Zuilen M, Hines R, and Foley CN (2004) Chromatographic separation and multicollection-ICPMS analysis of iron. Investigating mass-dependent and -independent isotope effects. Anal. Chem 76, 5855–5863. [PubMed: 15456307]

Davis AM and Grossman L (1979) Condensation and fractionation of rare earths in the solar nebula. Geochim. Cosmochim. Acta 43, 1611–1632.

Davis AM, Zhang J, Hu J, Greber ND, and Dauphas N (2018) Titanium isotopes and rare earth patterns in CAIs: evidence for thermal processing and gas-dust decoupling in the protoplanetary disk. Geochim. Cosmochim. Acta 221, 275–295.

Ebert S, Render J, Brennecka GA, Burkhardt C, Bischoff A, Gerber S, and Kleine T (2018) Ti isotopic evidence for a non-CAI refractory component in the inner Solar System. Earth Planet. Sci. Lett 498, 257–265.

Fagan TJ, Guan Y, and MacPherson GJ (2007) Al-Mg isotopic evidence for episodic alteration of Ca-Al-rich inclusions from Allende. Meteorit. Planet. Sci 42, 1221–1240.

Feng C, Qin T, Huang S, Wu Z, and Huang F (2014) First-principles investigations of equilibrium calcium isotope fractionation between clinopyroxene and Ca-doped orthopyroxene. Geochim Cosmochim Acta 143, 132–142.

Gall L, Williams HM, Halliday AN, and Kerr AC (2017) Nickel isotopic composition of the mantle. Geochim. Cosmochim. Acta 199, 196–209.

Gerber S, Burkhardt C, Budde G, Metzler K, and Kleine T (2017) Mixing and transport of dust in the early solar nebula as inferred from titanium isotope variations among chondrules. ApJL 841, L17.

Gussone N, Nehrke G, and Teichert BMA (2011) Calcium isotope fractionation in ikaite and vaterite. Chem. Geol 285, 194–202.

Habfast K (1983) Fractionation in the thermal ionization source. International Journal of Mass Spectrometry and Ion Physics 51, 165–189.

Hainebach KL, Clayton DD, Arnett WD, and Woosley SE (1974) On the e-process: its components and their neutron excesses. Astrophys. J 193, 157–168.

Hans U, Kleine T, and Bourdon B (2013) Rb-Sr chronology of volatile depletion in differentiated protoplanets: BABI, ADOR and ALL revisited. Earth Planet. Sci. Lett 374, 204–214.

Hart SR and Zindler A (1989) Isotope fractionation laws: a test using calcium. Int. J. Mass Spectr. Ion Proc 89, 287–301.

Hartmann D, Woosley SE, and El Eid MF (1985) Nucleosynthesis in neutron-rich supernova ejecta. Astrophys. J 297, 837–845.

Heuser A, Eisenhauer A, Gussone N, Bock B, Hansen BT, and Nägler TF (2002) Measurement of calcium isotopes (δ44Ca) using a multicollector TIMS technique. Int. J. Mass Spectrom 220, 385–397.

Heydegger HR, Foster JJ, and Compton W (1982) Terrestrial, meteoritic, and lunar Ti isotopic ratios revaluated: Evidence for correlated variations. Earth Planet. Sci. Lett 58, 406–418.

Hezel DC, Needham AW, and Russell SS (2008) Fe-isotopic composition of chondrules, CAI, matrix and bulk meteorite in Mokoia and Grosnaja CV-chondrites Lunar Planet. Sci. XXXIX Lunar Planet. Inst, Houston. #1603 (abstr.).

Huang S, Farkaš J, and Jacobsen SB (2010) Calcium isotopic fractionation between clinopyroxene and orthopyroxene from mantle peridotites. Earth Planet. Sci. Lett 292, 337–344.

Huang S, Farkaš J, Yu G, Petaev MI, and Jacobsen SB (2012) Calcium isotopic ratios and rare earth element abundances in refractory inclusions from the Allende CV3 chondrite. Geochim. Cosmochim. Acta 77, 252–265.

Kööp L, Davis AM, Nakashima D, Park C, Krot AN, Nagashima K, Tenner TJ, Heck PR, and Kita NT (2016) A link between oxygen, calcium, and titanium isotopes in ^{26}Al-poor hibonite-rich CAIs from Murchison and implications for the heterogeneity of dust reservoirs in the solar nebula. Geochim. Cosmochim. Acta 189, 70–95.

Krot AN, Scott ERD, and Zolensky ME (1995) Mineralogical and chemical modification of components in CV3 chondrites: nebular or asteroidal processing? Meteoritics 30, 748–775.

Krot AN, Nagashima K, Wasserburg GJ, Huss GR, Papanastassiou D, Davis AM, Hutcheon ID, and Bizzarro M (2014) Calcium-aluminum-rich inclusions with fractionation and unknown nuclear effects (FUN CAIs), I: mineralogy, petrology, and oxygen isotopic compositions. Geochim. Cosmochim. Acta 145, 206–247.

Kruijer TS, Kleine T, Fischer-Gódde M, Burkhardt C, and Wieler R (2014) Nucleosynthetic W isotope anomalies and the Hf-W chronometry of Ca-Al-rich inclusions. Earth Planet. Sci. Lett 403, 317–327.

Larsen KK, Trinquier A, Paton C, Schiller M, Wielandt D, Ivanova MA, Connelly JN, Nordlund A, Krot AN, and Bizzarro M (2011) Evidence for magnesium isotope heterogeneity in the solar protoplanetary disk. Astrophys. J 735, L37–L44.

Lee T, Russell WA, and Wasserburg GJ (1979) Calcium isotopic anomalies and the lack of aluminum-26 in an unusual Allende inclusion. Astrophys. J 228, L93–L98.

Leya I, Schönbächler M, Krähenbühl U, and Halliday AN (2009) New titanium isotope data for Allende and Efremovka CAIs. Astrophys. J 702, 1118–1126.

Liu P-P, Zhou M-F, Luais B, Cividini D, and Rollion-Bard C (2014) Disequilibrium iron isotopic fractionation during the high-temperature magmatic differentiation of the Baima Fe-Ti oxide-bearing mafic intrusion, SW China. Earth Planet. Sci. Lett 399, 21–29.

Lodders K (2003) Solar system abundances and condensation temperatures of the elements. Astrophys. J 591, 1220–1247.

Loss RD and Lugmair GW (1990) Zinc isotope anomalies in Allende meteorite inclusions. Astrophys. J 360, L59–L62.

Mane P, Romaniello SJ, Brennecka GA, Williams CD, and Wadhwa M (2014) Zr isotope systematics of Allende CAIs Meteoritical Society Meeting LXXVII. Lunar Planet. Inst, Casablanca. #5403 (abstr.).

Mane P, Torrano ZA, Romaniello SJ, Brennecka GA, Shollenberger QR, Borg L, and Wadhwa M (2016) Zirconium and Chromium isotope systematics of non-Allende CAIs Lunar Planet. Sci. XLVII Lunar Planet. Inst, Houston. #2778 (abstr.).

Mercer C, Souders AK, Romaniello SJ, Williams CD, Brennecka GA, and Wadhwa M (2015) Chromium and titanium isotope systematics of Allende CAIs Lunar Planet. Sci. XLVI Lunar Planet. Inst, Houston. #2920 (abstr.).

Millet M-A. and Dauphas N. (2014) Ultra-precise titanium stable isotope measurements by double-spike high resolution MC-ICP-MS. J. Anal. At. Spectrom 29, 1444–1458.

Moynier F, Day JMD, Okui W, Yokoyama T, Bouvier A, Walker RJ, and Podosek FA (2012) Planetary-scale strontium isotope heterogeneity and the age of volatile depletion of early Solar System materials. Astrophys. J 758, 45–52.

Mullane E, Russell SS, and Gounelle M (2005) Nebular and asteroidal modification of the iron isotope composition of chondritic components. Earth Planet. Sci. Lett 239, 203–218.

Myojo K, Yokoyama T, Okabayashi S, Wakaki S, Sugiura N, and Iwamori H (2018) The origin and evolution of nucleosynthetic Sr isotope variability in calcium and aluminum-rich refractory inclusions. Astrophys. J 853, 48–56.

Niederer FR and Papanastassiou DA (1984) Ca isotopes in refractory inclusions. Geochim. Cosmochim. Acta 48, 1279–1293.

Niederer FR, Papanastassiou DA, and Wasserburg GJ (1980) Endemic isotopic anomalies in titanium. Astrophys. J 240, 73–77.

Niederer FR, Papanastassiou DA, and Wasserburg GJ (1981) The isotopic composition of Ti in the Allende and Leoville meteorites. Geochim. Cosmochim. Acta 45, 1017–1031.

Niederer FR, Papanastassiou DA, and Wasserburg GJ (1985) Absolute isotopic abundances of Ti in meteorites. Geochim. Cosmochim. Acta 49, 835–851.

Niemeyer S and Lugmair GW (1981) Ubiquitous isotopic anomalies in Ti from normal Allende inclusions. Earth Planet. Sci. Lett 53, 211–225.

Nittler LR (2003) Presolar stardust in meteorites: recent advances and scientific frontiers. Earth Planet. Sci. Lett 209, 259–273.

Nittler LR, Alexander CMO, Liu N, and Wang J (2018) Extremely ^{54}Cr- and ^{50}Ti-rich presolar oxide grains in a primitive meteorite: formation in rare types of supernovae and implications for the astrophysical context of solar system birth. Astrophys. J 856, L24–L30.

Ockert C, Gussone N, Kaufhold S, and Teichert BMA (2013) Isotope fractionation during Ca exchange on clay minerals in a marine environment. Geochim. Cosmochim. Acta 112, 374–388.

Oeser M, Dohmen R, Horn I, Schuth S, and Weyer S (2015) Processes and time scales of magmatic evolution as revealed by Fe-Mg chemical and isotopic zoning in natural olivines. Geochim. Cosmochim. Acta 154, 130–150.

Oeser M, Weyer S, Horn I, and Schuth S (2014) High-precision Fe and Mg isotope ratios of silicate reference glasses determined in situ by femtosecond LA-MC-ICP-MS and by solution nebulisation MC-ICP-MS. Geostand. Geoanalytical Res 38, 311–328.

Papanastassiou DA and Brigham CA (1989) The identification of meteorite inclusions with isotope anomalies. Astrophys. J 338, L37–L40.

Paton C, Schiller M, and Bizzarro M (2013) Identification of an ^{84}Sr-Depleted carrier in primitive meteorites and implications for thermal processing in the solar protoplanetary disk. ApJL 763, L40–L46.

Quitté G, Halliday AN, Meyer BS, Markowski A, Latkoczy C, and Günther D (2007) Correlated Iron 60, Nickel 62 and Zirconium 96 in refractory inclusions and the origin of the Solar System. Astrophys. J 655, 678–684.

Render J, Brennecka GA, Wang S, Wasylenki LE, and Kleine T (2018) A distinct nucleosynthetic heritage for early Solar System solids recorded by Ni isotope signatures. Astrophys. J 862, 1–18.

Richter S, Eykens R, Kühn H, Aregbe Y, Verbruggen A, and Weyer S (2010) New average values for the n(238U)/n(235U) isotope ratios of natural uranium standards. International Journal of Mass Spectrometry 295, 94–97.

Rosman KJR and Taylor PDP (1998) Isotopic compositions of the elements 1997 (Technical Report) Pure Appl. Chem 70, 217–235.

Rout SS and Bischoff A (2008) Ca,Al-rich inclusions in Rumuruti (R) chondrites. MAPS 9, 1439–1464.

Russell WA and Papanastassiou DA (1978) Calcium isotope fractionation in ion-exchange chromatography. Anal. Chem 50, 1151–1154.

Russell WA, Papanastassiou DA, and Tombrello TA (1978) Ca isotope fractionation on the Earth and other solar system materials. Geochim. Cosmochim. Acta 42, 1075–1090.

Ruzicka A, Floss C, and Hutson M (2012) Amoeboid olivine aggregates (AOAs) in the Efremovka, Leoville and Vigarano (CV3) chondrites: A record of condensate evolution in the solar nebula. Geochim. Cosmochim. Acta 79, 79–105.

Ryu J-S, Jacobson AD, Holmden C Lundstrom C, and Zhang Z (2011) The major ion, $\delta^{44/40}$Ca, $\delta^{44/42}$Ca, and $\delta^{26/24}$Mg geochemistry of granite weathering at pH = 1 and T = 25 °C: power-law processes and the relative reactivity of minerals. Geochim. Cosmochim. Acta 75, 6004–6026.

Schiller M, Paton C, and Bizzarro M (2015) Evidence for nucleosynthetic enrichment of the protosolar molecular cloud core by multiple supernova events. Geochim. Cosmochim. Acta 149, 88–102. [PubMed: 25684790]

Schiller M, Gussone N, and Wombacher F (2016) High temperature geochemistry and cosmochemistry In: Calcium stable isotope geochemistry. Advances in isotope geochemistry. Springer, Berlin, Heidelberg.

Schuth S, Hurraß J, Münker C, and Mansfeldt T (2015) Redox-dependent fractionation of iron isotopes in suspensions of a groundwater-influenced soil. Chem. Geol 392, 74–86.

Shollenberger QR, Borg LE, Render J, Ebert S, Bischoff A, Russell SS, and Brennecka GA (2018a) Isotopic coherence of refractory inclusions from CV and CK meteorites: Evidence from multiple isotope systems. Geochim. Cosmochim. Acta 228, 62–80.

Shollenberger QR, Render J, and Brennecka GA (2018b) Er, Yb, and Hf isotopic compositions of refractory inclusions: An integrated isotopic fingerprint of the Solar System's earliest reservoir. Earth Planet. Sci. Lett 495, 12–23.

Simon JI, Jordan MK, Tappa MJ, Schauble EA, Kohl IE, and Young ED (2017) Calcium and titanium isotope fractionation in refractory inclusions: Tracers of condensation and inheritance in the early solar protoplanetary disk. Earth Planet. Sci. Lett 472, 277–288.

Sio CK, Dauphas N, Teng F-Z, Chaussidon M, Helz RT, and Roskosz M (2013) Discerning crystal growth from diffusion profiles in zoned olivine by in situ Mg-Fe isotopic analyses. Geochim. Cosmochim. Acta 123, 302–321.

Spivak-Birndorf L, Wadhwa M, and Janney P (2009) 26Al–26Mg systematics in D'Orbigny and Sahara 99555 angrites: Implications for high-resolution chronology using extinct chronometers. Geochim. Cosmochim. Acta 73, 5202–5211.

Tang H and Dauphas N (2012) Abundance, distribution, and origin of ^{60}Fe in the solar protoplanetary disk. Earth Planet. Sci. Lett 248, 248–263.

Taylor p.D.P., Maeck R, and De Bievre P (1992) Determination of the absolute isotopic composition and atomic weight of a reference sample of natural iron. Int. J. Mass Spectrom. Ion Processes 121, 111–125.

Thrane K, Bizzarro M, and Baker JA (2006) Extremely brief formation interval for refractory inclusions and uniform distribution of ^{26}Al in the early solar system. Astrophys. J 646, L159–L162.

Tissot FLH, Dauphas N, and Grossman W (2016) Origin of uranium isotope variations in early solar nebula condensates. Sci. Adv 2, e1501400. [PubMed: 26973874]

Torrano ZA, Rai VK, and Wadhwa M (2018) Combined investigation of chromium, titanium, and magnesium isotope compositions of refractory inclusions from a variety of carbonaceous chondrites Lunar Planet. Sci. XLIX Lunar Planet. Inst, Houston. #2405 (abstr.).

Trinquier A, Elliott T, Ulfbeck D, Coath C, Krot AN, and Bizzarro M (2009) Origin of nucleosynthetic isotope heterogeneity in the solar protoplanetary disk. Science 324, 374–376. [PubMed: 19372428]

Völkening J and Papanastassiou DA (1989) Iron isotope anomalies. ApJ 347, L43–L46.

Wark DA and Lovering JF (1982) The nature and origin of type B1 and B2 Ca-Al-rich inclusions in the Allende meteorite. Geochim. Cosmochim. Acta 46, 2581–2594.

Wang S and Wasylenki LE (2017) Experimental constraints on reconstruction of Archean seawater Ni isotopic composition from banded iron formations. Geochim. Cosmochim. Acta 206, 137–150.

Wasserburg GJ, Lee T, and Papanastassiou DA (1977) Correlated O and Mg isotopic anomalies in Allende inclusions, II: Magnesium Geophys. Res. Letters 4, 299–302.

Wasserburg GJ, Wimpenny J, and Yin Q-Z (2012) Mg isotopic heterogeneity, Al-Mg isochrons, and canonical ^{26}Al/^{27}Al in the early solar system. Meteorit. Planet. Sci 12, 1980–1997.

Wasserburg GJ, Trippella O, and Busso M (2015) Isotope anomalies in the Fe-group elements in meteorites and connections to nucleosynthesis in AGB stars. ApJ 805, 7–25.

Wasylenki LE, Howe HD, Spivak-Birndorf LJ, and Bish DL (2014) Ni isotope fractionation during sorption to ferrihydrite: Implications for Ni in banded iron formations. Chem. Geol 400, 56–64.

Weyer S, Anbar AD, Brey GP, Münker C, Mezger K, and Woodland AB (2005) Iron isotope fractionation during planetary differentiation. Earth Planet. Sci. Lett 240, 251–264.

Weyer S, Anbar AD, Gerdes A, Gordon GW, Algeo TJ, and Boyle EA (2008) Natural fractionation of 238U/235U. Geochim. Cosmochim. Acta 72, 345–359.

Williams CD, Janney PE, Hines RR, and Wadhwa M (2016) Precise titanium isotope compositions of refractory inclusions in the Allende CV3 chondrite by LA-MC-ICPMS. Chem. Geol 436, 1–10.

Zhang J, Dauphas N, Davis AM, and Pourmand A (2011) A new method for MC-ICPMS measurement of titanium isotopic composition: Identification of correlated isotope anomalies in meteorites. J. Anal. At. Spectrom 26, 2197–2205.

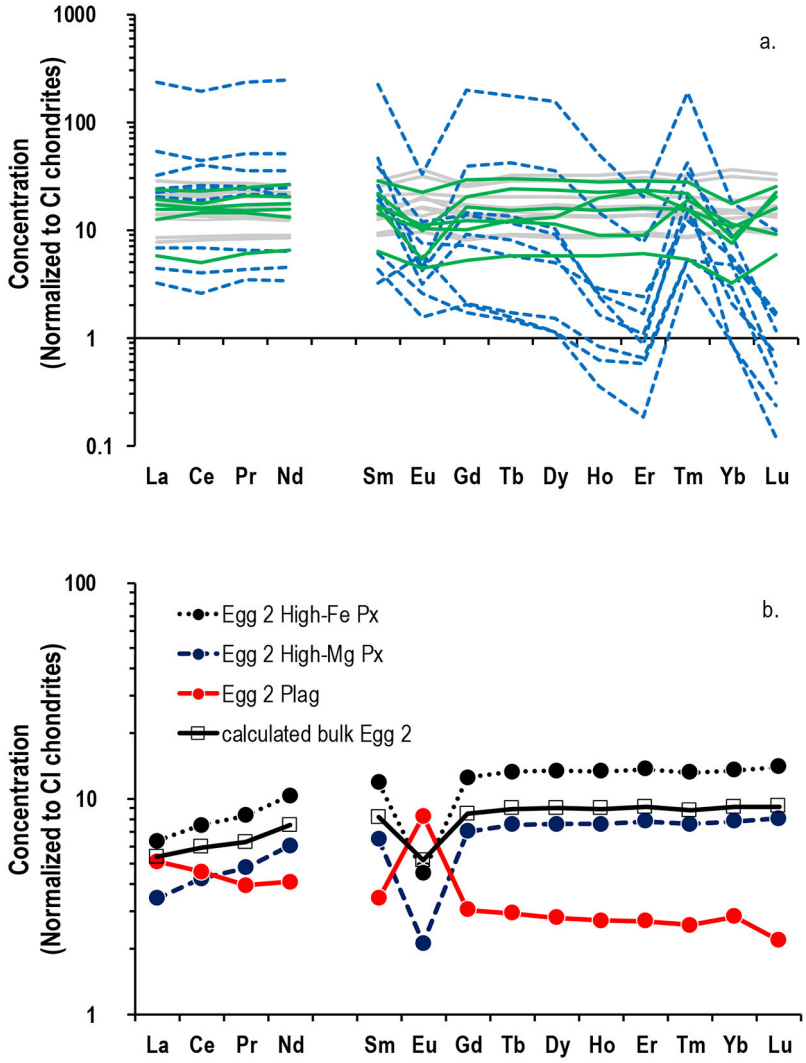

Figure 1.

a) Rare earth element (REE) patterns of the bulk CAIs studied here are variable and are indicative of their condensation and evaporation histories. The CAIs with unfractionated REE patterns are shown in grey, while those with group II REE patterns are displayed as dashed blue lines. CAIs with group III patterns are in green. b) The REE patterns of Egg 2 mineral separates are shown along with a calculated bulk Egg 2 pattern. All three mineral separates have relatively unfractionated HREE patterns but have LREE patterns and Eu anomalies characteristic of the minerals pyroxene and plagioclase. Data normalized to REE abundances in CI chondrites (Lodders, 2003). Note that REE data for CAI A-ZH-1 was not measured and as such is not shown here.

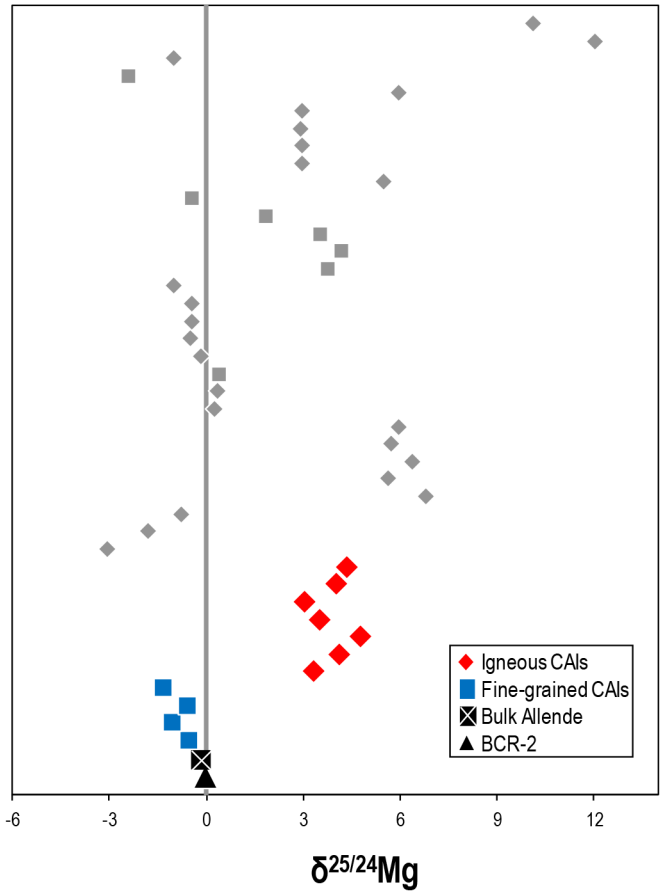

Figure 2.

The mass-dependent Mg isotopic compositions of CAIs, BCR-2, and bulk Allende reported in this study (colored symbols). Literature data are shown in grey (Bizzarro et al., 2004; Thrane et al., 2006; Larsen et al., 2011; Wasserburg et al., 2012); diamonds indicate igneous CAIs whereas squares indicate fine-grained CAIs. Uncertainties in all cases are smaller than the symbols. The vertical grey bar represents the 2SD of repeat analyses of the terrestrial standard during the measurement campaign.

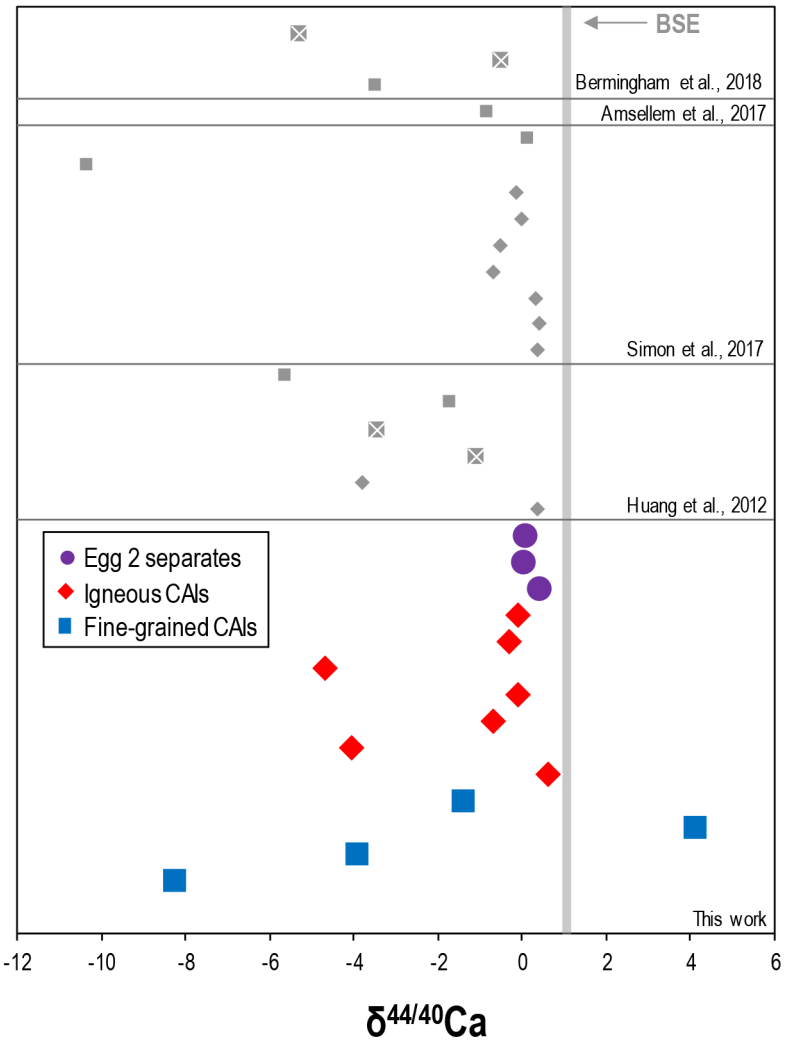

Figure 3.

The mass-dependent Ca isotopic compositions of the CAIs and Egg 2 mineral separates relative to SRM915a. The bulk silicate earth (BSE) $\delta^{44/40}$Ca of +1.05 ± 0.04 (defined by Huang et al., 2010) is represented by the vertical grey bar. Literature data are shown as grey symbols; diamonds indicate igneous CAIs whereas squares indicate fine-grained CAIs, and CAIs that have not been identified as fine-grained or igneous are shown as grey squares with white crosses (Huang et al., 2012; Amsellem et al., 2017; Simon et al., 2017; Bermingham et al., 2018). Uncertainties are smaller than the symbols.

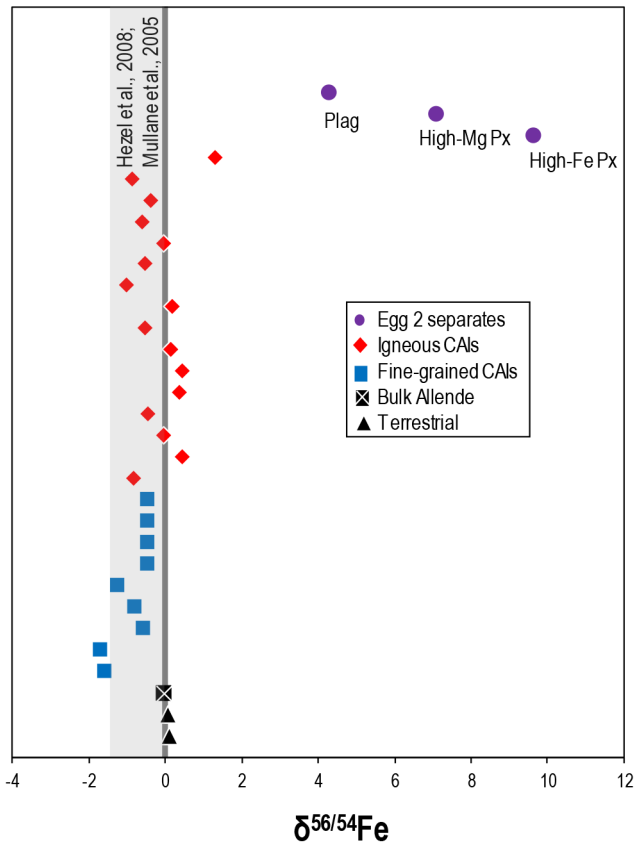

Figure 4.

The mass-dependent Fe isotopic compositions of the CAIs, mineral separates, bulk Allende, and terrestrial rock standards. The vertical dark grey bar represents the 2SD of repeat analyses of the terrestrial standard during the measurement campaign and the vertical light grey band is literature CAI data (Hezel et al., 2008; Mullane et al., 2005). Data are externally normalized using $^{63}Cu/^{65}Cu = 2.24359$ to correct for instrumentally induced mass bias (see main text). Analytical uncertainties are smaller than the symbols.

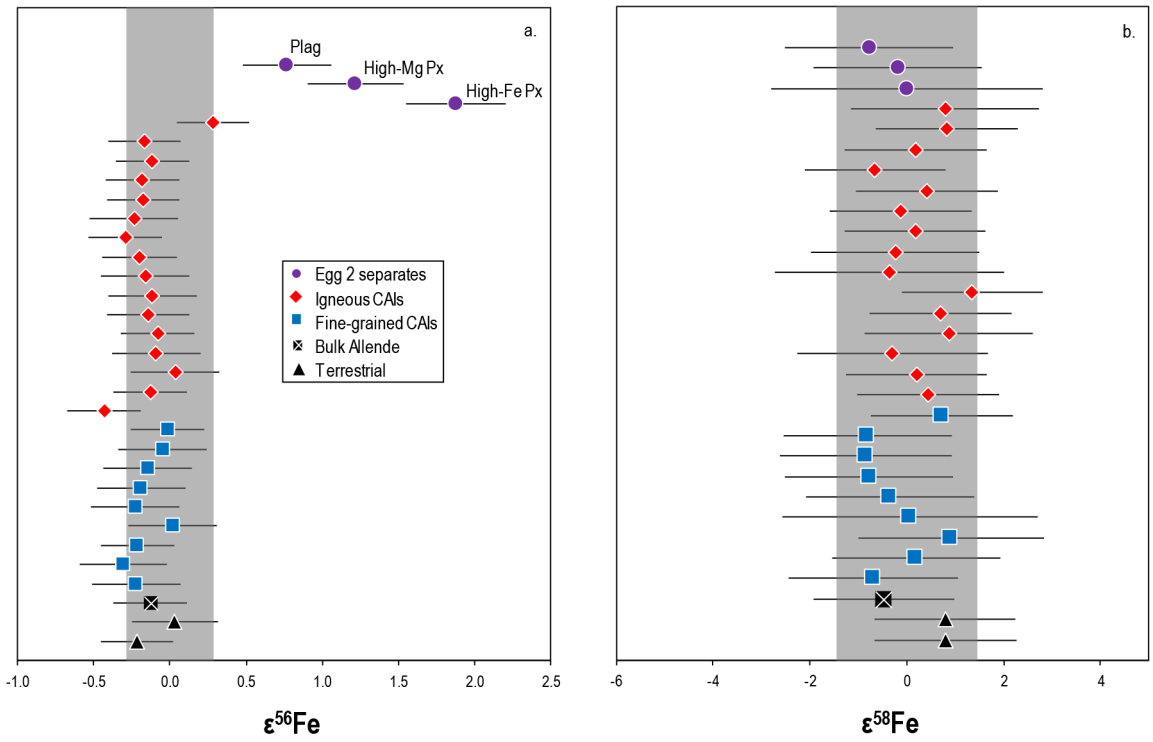

Figure 5.

The nucleosynthetic a) ε^{56}Fe and b) ε^{58}Fe compositions of the CAIs, mineral separates, bulk Allende, and the terrestrial rock standards. Individual uncertainties represent either the long-term reproducibility, which is the 2× standard deviation (2SD) of repeat analyses of the IRMM-014 Fe reference material run at equivalent concentration, or the 2SD of repeat analyses of the sample, whichever was larger. The vertical grey band in each of the plots represents the 2SD of repeat analyses of the IRMM-014 Fe reference material over the measurement campaign. Data are internally normalized to ^{57}Fe/^{54}Fe = 0.36255 (Taylor et al., 1992).

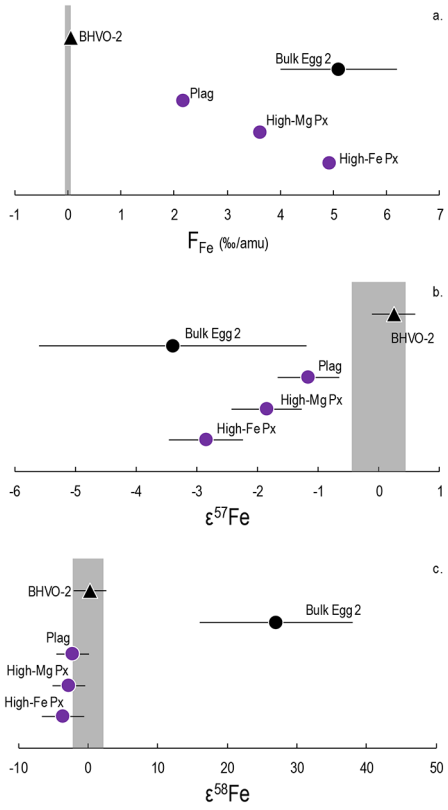

Figure 6.

a) Isotope fractionation (FFe) in $‰_0$/amu, b) ε^{57}Fe, and c) ε^{58}Fe values in the Egg 2 mineral separates (purple circles) and BHVO-2 (black triangle). The ε^{57}Fe and ε^{58}Fe values are obtained by internal normalization to $^{56}Fe/^{54}Fe = 15.69786$ (Rosman and Taylor, 1998) for direct comparison with Völkening and Papanastassiou (1989). The mineral separates display deficits in ε^{57}Fe relative to the terrestrial composition; no isotopic variations are observed outside analytical uncertainty for ε^{58}Fe. Individual uncertainties represent the 2SD of repeat analyses of the terrestrial standard or of repeat sample analyses, whichever was larger. The ε^{57}Fe and ε^{58}Fe have a second-order mass fractionation correction following Render et al. (2018). For comparison, the bulk Egg 2 data from Völkening and Papanastassiou, (1989) are also shown (black circle).

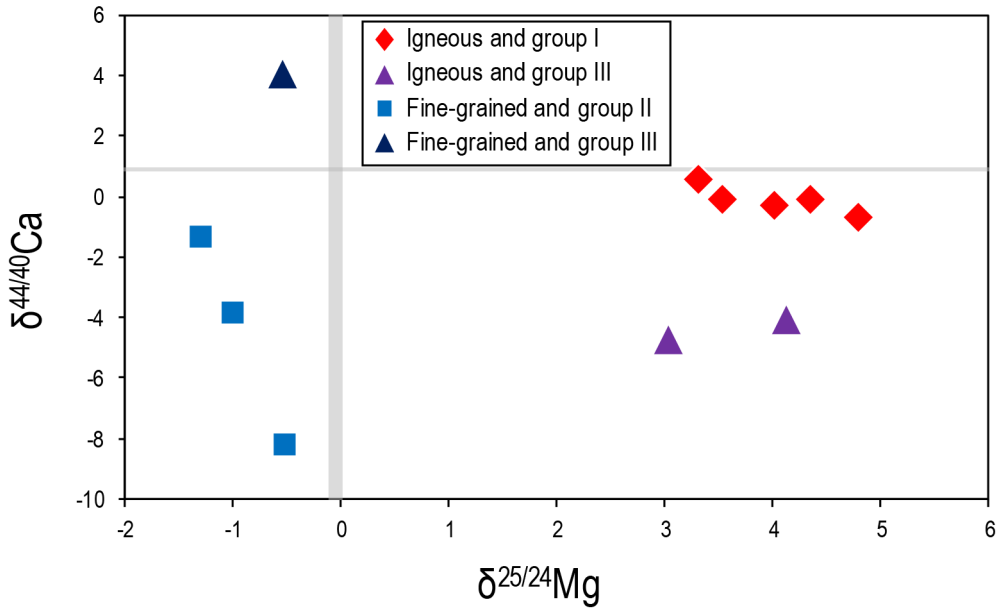

Figure 7.

The mass-dependent Ca isotopic compositions of the CAIs versus mass-dependent Mg isotopic compositions. Grey bars represent the BSE as determined from BCR-2 and BHVO-2 in this work. Uncertainties are smaller than the symbols.

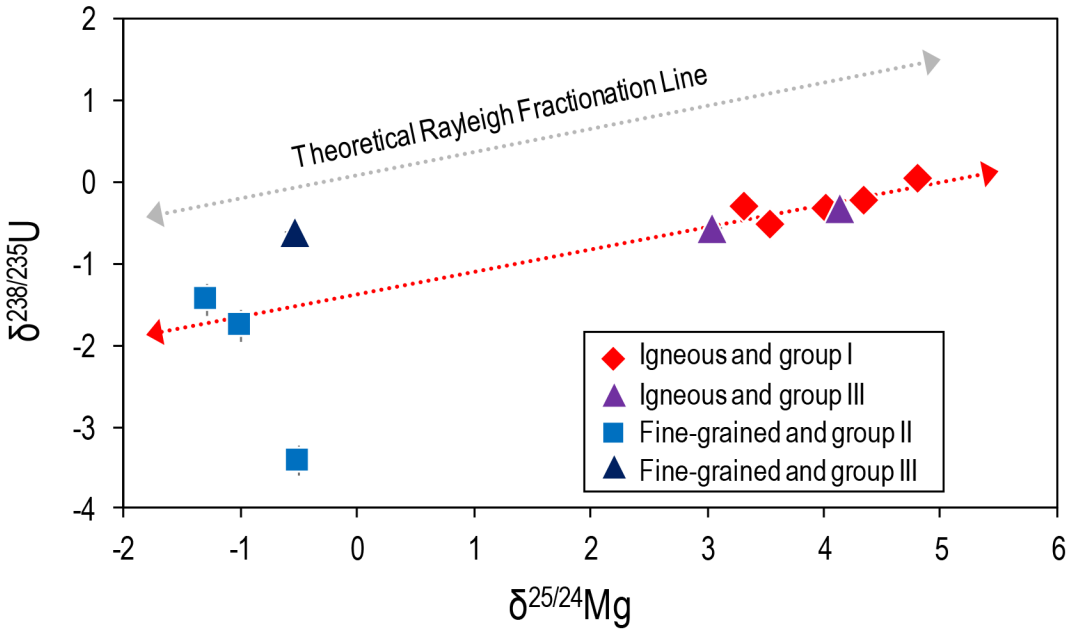

Figure 8.

The U isotope compositions (expressed as $\delta^{238/235}U$) versus the mass-dependent Mg isotopic compositions of CAIs. The U isotopic compositions are from Brennecka et al. (2010) and are corrected for the updated U isotope composition of the SRM950a standard (Richter et al., 2010). The dotted red line is a regression through the igneous CAIs only, whereas the grey dotted line is a theoretical Rayleigh fractionation line. Uncertainties are shown as the 2SD of repeat analyses of the terrestrial standard and are smaller than the symbol when not visible.

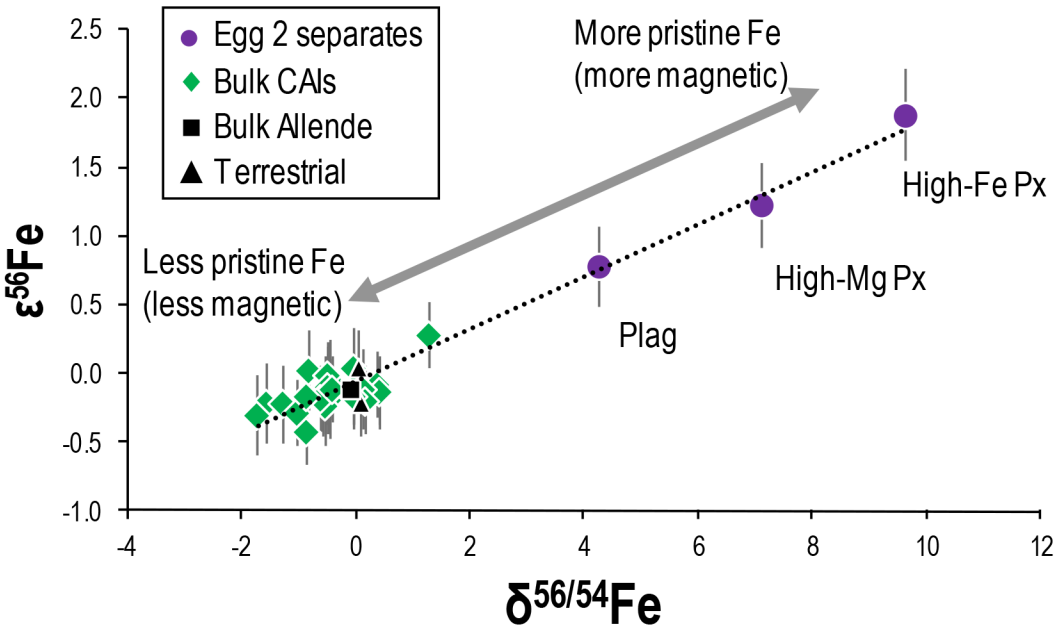

Figure 9.

Plot of the nucleosynthetic (ε^{56}Fe) compositions versus the mass-dependent ($\delta^{56/54}$Fe) compositions of the Egg 2 mineral separates (purple circles), bulk CAIs (green diamonds), bulk Allende (black square), and terrestrial rock standards (black triangles). Uncertainties on individual data points represent the 2× standard deviation (2SD) of the long-term reproducibility of the IRMM-014 Fe reference material run at equivalent concentration or the 2SD of the sample analyses, whichever was larger. The dashed black line is a best fit to the data.

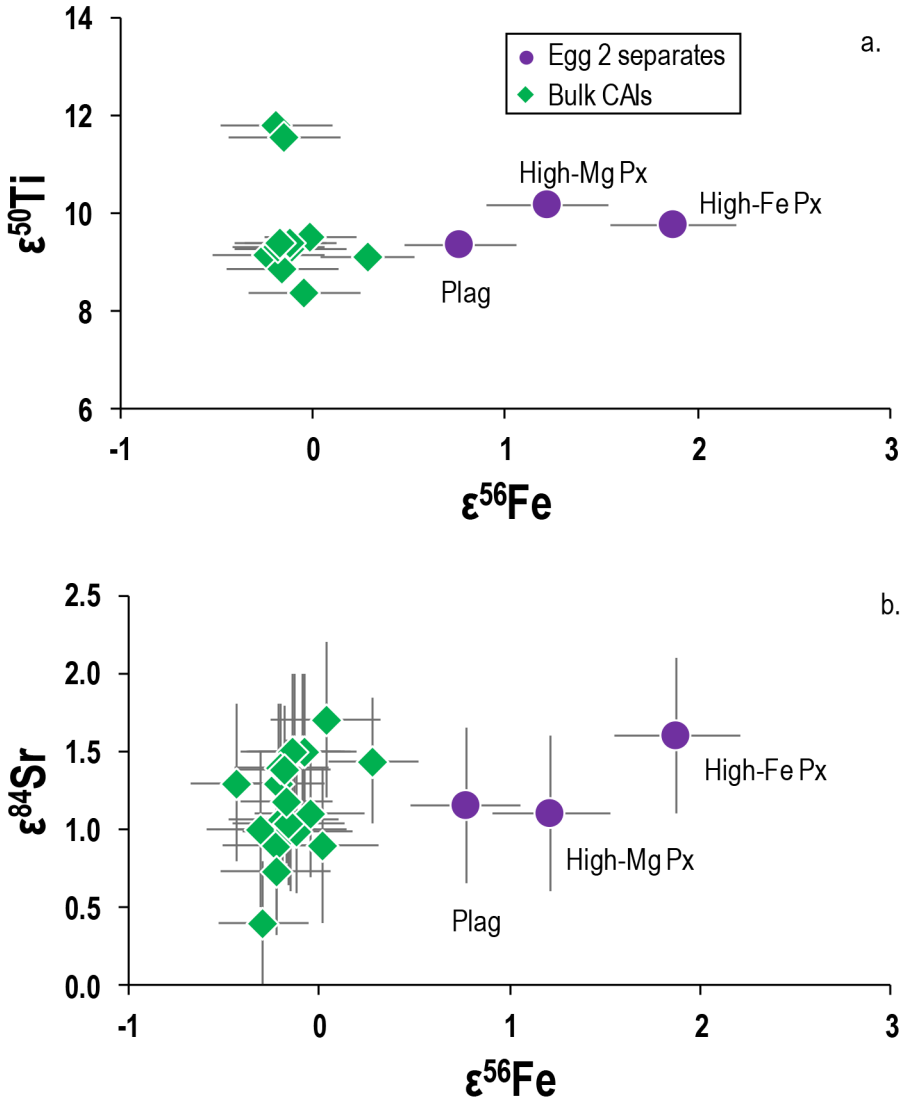

Figure 10.

Plots of a) ε^{50}Ti versus ε^{56}Fe and b) ε^{84}Sr versus ε^{56}Fe for the Egg 2 mineral separates and the bulk CAIs. Literature CAI data from Brennecka et al. (2013), Brennecka et al. (2017b), and Shollenberger et al. (2018). Symbols are the same as in Fig. 9.

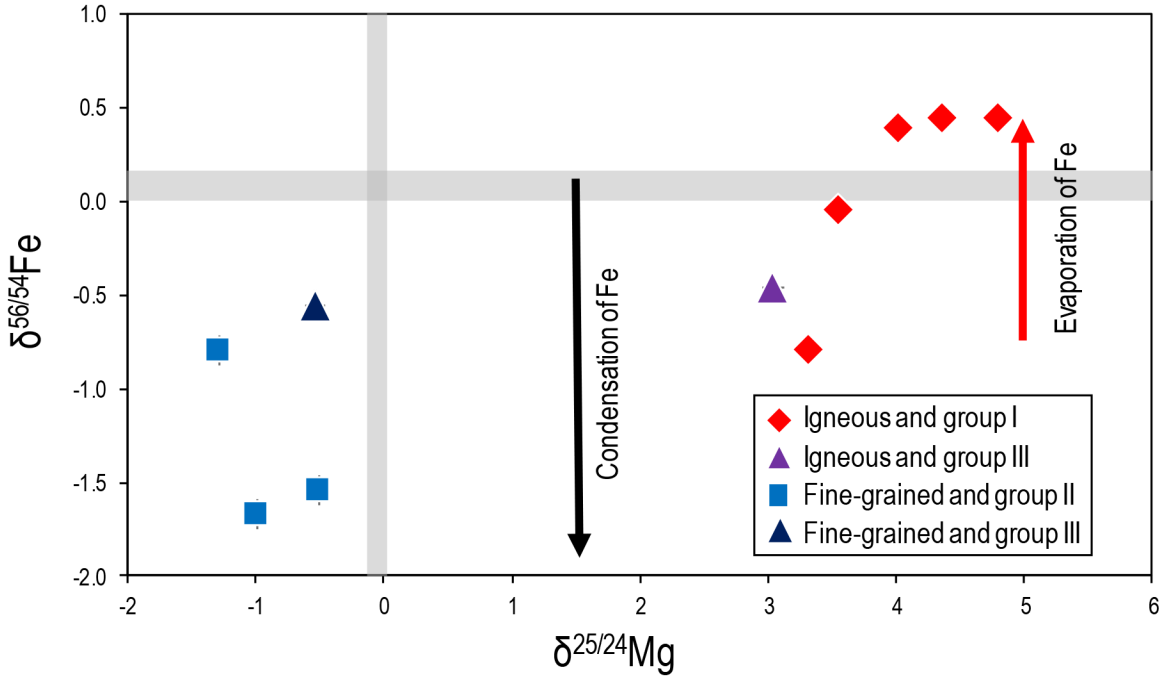

Figure 11.

The mass-dependent Fe isotope compositions of the CAIs versus their mass-dependent Mg isotope compositions. Grey bars represent the BSE as determined from BCR-2 and BHVO-2 in this work. Uncertainties are shown for as the 2SD of repeat analyses of the terrestrial standard and are smaller than the symbol when not visible.

Table 1.

Description of the Egg 2 mineral separates and CAIs analyzed in this study.

Sample	Host meteorite	Mass (mg)	Description	REE pattern	Previously investigated isotope systems*	Digestion	Initial reference
Egg 2 Plag	Allende (CV3)	55	plagioclase/Ig/B	-	-	hot plate/[ND]	this work
Egg 2 high-Mg Px	Allende (CV3)	38	high-Mg Px/Ig/B	-	-	hot plate/[ND]	this work
Egg 2 high-Fe Px	Allende (CV3)	89	high-Fe Px/Ig/B	-	-	hot plate/[ND]	this work
164	Allende (CV3)	705	B/Ig	Group I	Ti, Ni, Zr, Sr, Mo, Te, Ba, Nd, Sm, Er, Yb, Hf, U	PDS/[PD]	[1]
165	Allende (CV3)	2,838	B/A1/Ig	Group III	Ti, Cr, Ni, Zr, Sr, Mo, Te, Ba, Nd, Sm, Er, Yb, Hf, U	PDS/[PD]	[1]
166	Allende (CV3)	173	FG	Group II	Ti, Cr, Ni, Zr, Sr, Te, Ba, Nd, Sm, U	PDS/[PD]	[1]
167	Allende (CV3)	368	FG	Group II	Ti, Cr, Ni, Zr, Sr, Te, Nd, Sm, U	PDS/[PD]	[1]
168	Allende (CV3)	1,343	A/Ig	Group I	Ti, Cr, Ni, Zr, Sr, Te, Ba, Nd, Sm, Er, Yb, Hf, U	PDS/[PD]	[1]
170	Allende (CV3)	199	B1/Ig	Group I	Ti, Zr, Sr, Mo, Te, Ba, Nd, Sm, Er, Yb, U	PDS/[PD]	[1]
171	Allende (CV3)	199	B/Ig	group III	Ti, Ni, Zr, Sr, Te, Ba, Nd, Sm, Er, Yb, U	PDS/[PD]	[1]
172	Allende (CV3)	441	B/Ig	Group I	Ti, Ni, Zr, Sr, Mo, Te, Ba, Nd, Sm, Er, Yb, Hf, U	PDS/[PD]	[1]
173	Allende (CV3)	607	altered A/FG	Group III	Ti, Cr, Ni, Zr, Sr, Mo, Te, Ba, Nd, Sm, Er, Yb, Hf, U	PDS/[PD]	[1]
174	Allende (CV3)	441	B/Ig	Group I	Ti, Zr, Sr, Mo, Te, Ba, Nd, Sm, Er, Yb, Hf, U	PDS/[PD]	[1]
175	Allende (CV3)	310	FG	Group II	Ti, Cr, Ni, Zr, Sr, Te, Ba, Nd, Sm, U	PDS/[PD]	[1]
AF01	Allende (CV3)	289	FG	Group II	Ti, Ni, Sr, Mo, Ba, W	hot plate/[PD]	[2]
AF02	Allende (CV3)	120	FG	Group II	Ti, Ni, Sr, Mo, Ba, W	hot plate/[PD]	[2]
AF03	Allende (CV3)	34	FG	Group II	Ti, Ni, Sr, Mo, Ba, W	hot plate/[PD]	[2]
AF04	Allende (CV3)	288	FG	Group II	Ti, Ni, Sr, Mo, Ba, W	hot plate/[PD]	[2]
A-ZH-1	Allende (CV3)	120	B/Ig	-	Ti, Ni, Sr, Mo, W	hot plate/[PD]	[3]
A-ZH-2	Allende (CV3)	180	B/Ig	Group I	Ti, Ni, Sr, Mo, Er, Yb, W	hot plate/[PD]	[3]
A-ZH-3	Allende (CV3)	70	B/Ig	Group I	Ti, Ni, Mo, W	hot plate/[PD]	[3]
A-ZH-4	Allende (CV3)	200	B/Ig	Group I	Ti, Ni, Sr, Mo, Er, Yb, W	hot plate/[PD]	[3]
A-ZH-5	Allende (CV3)	90	fluffy A/FG	Group III	Ti, Ni, Mo, Nd, Sm, W	hot plate/[PD]	[3]
AI01	NWA 6870 (CV3)	82	B/Ig	Group I	Ti, Ni, Sr, Mo, Ba, Hf, W	hot plate/[PD]	[2]
AI02	NWA 6717 (CV3)	103	B/Ig	Group II	Ti, Ni, Sr, Mo, Ba, W	hot plate/[PD]	[2]
Lisa	NWA 6991 (CV3)	53	B1/Ig	Group V	Ti, Cr, Ni, Zr, Sr, Mo, Ba, Nd, Sm, Er, Yb	Parr bomb/[PD]	[4]
Marge	NWA 6619 (CV3)	112	related to B/Ig	Group III/EV?	Ti, Cr, Ni, Zr, Sr, Mo, Ba, Nd, Sm, Er, Yb	Parr bomb/[PD]	[4]
Bart	NWA 6254 (CK3)	69	related to C/Ig	Group III	Ti, Cr, Ni, Zr, Sr, Mo, Ba, Nd, Sm, Er, Yb	Parr bomb/[PD]	[4]

Sample	Host meteorite	Mass (mg)	Description	REE pattern	Previously investigated isotope systems*	Digestion	Initial reference
Homer	NWA 4964 (CK3)	136	related to C/Ig	Group II	Ti, Cr, Ni, Zr, Sr, Mo, Ba, Nd, Sm, Yb	Parr bomb/[PD]	[4]

The last column provides the initial reference for each CAI sample ([1] Brennecka et al., 2010; [2] Kruijer et al., 2014; [3] Burkhardt et al., 2008; [4] Shollenberger et al., 2018a).

*Isotope data for the elements indicated here are given in: Brennecka et al., 2010, 2013, 2017a, 2017b; Kruijer et al., 2014; Burkhardt et al., 2008, 2011, 2016; Mane et al., 2014, 2016; Mercer et al., 2015; Shollenberger et al., 2018a, 2018b; Render et al., 2018; Torrano et al., 2018.

Plag = plagioclase, high-Mg Px = high magnesium pyroxene, high-Fe Px = high iron pyroxene, FG = fine-grained, Ig = igneous, B = Type B, B1 = Type B1, A = Type A, A1= Type A1, related to B = related to Type B, related to C = related to Type C, altered A = altered Type A, fluffy A = fluffy Type A, PDS = pressure digestion system (PicoTrace), ND = new digestion, PD = previously digested.

Table 2.

Cup configuration for Fe isotopic analyses.

Cup	L4	L3	L2	L1	C*	H1	H2	H3	H4
Line 1					$^{56}Fe^{a}$				
Line 2		^{63}Cu		^{65}Cu					
Line 3		^{53}Cr	^{54}Fe	^{55}Mn	^{56}Fe	^{57}Fe	^{58}Fe		^{60}Ni

*denotes 10^{10} ohm resistor

[a]denotes a peak center on ^{56}Fe and not the ^{56}Fe shoulder (*i.e.,* $^{55.9}Fe$)

Table 3.

Mass-dependent Mg, Ca, and Ni isotope compositions along with U isotope compositions of the investigated samples and standards.

Sample	Notes	$\delta^{25/24}$Mg	2SD	$\delta^{26/24}$Mg	2SD	$\delta^{44/40}$Ca	2SD	$\delta^{60/58}$Ni	2SD	$\delta^{238/235}$U	2SD
Egg 2 Plag	ND	-	-	-	-	0.05	0.14	3.86	0.06	−0.32	0.16
Egg 2 high-Mg Px	ND	-	-	-	-	0.02	0.08	3.94	0.06	−0.36	0.16
Egg 2 high-Fe Px	ND	-	-	-	-	0.40	0.14	4.24	0.06	−0.38	0.16
Egg 2 bulk	ND	-	-	-	-	-	-	*4.15*	*0.06*	-	-
CAI 164	PUC	3.32	0.09	7.30	0.18	0.60	0.08	*0.21*	*0.06*	*−0.30*	0.12
CAI 165	PUC	4.13	0.06	9.07	0.11	−4.06	0.08	*1.94*	*0.06*	*−0.33*	*0.11*
CAI 166	PC	−0.50	0.05	−0.04	0.09	−8.28	0.08	*−0.08*	*0.06*	*−3.42*	*0.28*
CAI 167	PC	−0.99	0.05	−1.28	0.09	−3.93	0.12	*0.28*	*0.06*	*−1.76*	*0.30*
CAI 168	PUC	4.80	0.06	10.49	0.14	−0.68	0.08	*1.63*	*0.06*	*0.04*	*0.11*
CAI 170	PC	3.54	0.06	7.88	0.06	−0.11	0.08	-	-	*−0.51*	*0.28*
CAI 171	PC	3.04	0.04	6.69	0.08	−4.70	0.08	-	-	*−0.56*	*0.22*
CAI 172	PC	4.02	0.06	8.81	0.12	−0.31	0.23	-	-	*−0.31*	*0.28*
CAI 173	PC	−0.54	0.05	0.08	0.06	4.10	0.08	*0.31*	*0.06*	*−0.61*	*0.28*
CAI 174	PC	4.35	0.07	9.51	0.11	−0.09	0.08	-	-	*−0.23*	*0.11*
CAI 175	PC	−1.28	0.09	−2.22	0.20	−1.40	0.08	*0.22*	*0.06*	*−1.45*	*0.22*
Bulk Allende	-	−0.15	0.09	−0.28	0.22	*0.55*	*0.11*	*0.242*	*0.073*	*−0.45*	*0.11*
BHVO-2	-	-	-	-	-	0.90	0.08	0.19	0.10	-	-
BCR-2	-	−0.05	0.07	−0.09	0.11	-	-	0.26	0.06	*−0.27*	*0.19*

The uncertainties shown represent the 2SD of replicate sample analyses or the external reproducibilities (2SD) of the method. Data from the literature is shown in italics: bulk CAI Ni data is from Render et al. (2018), bulk Allende Ni data is from Gall et al. (2017), and bulk Allende Ca data is from Simon et al. (2017). Uranium isotope compositions of bulk CAIs are from Brennecka et al. (2010) and are corrected for the updated SRM950a standard value ($^{238}U/^{235}U = 137.837$) (Richter et al., 2010).

Px = pyroxene, Plag = plagioclase, ND = new digestion, PUC = previously experienced only uranium ion chromatography, PC = previous ion chromatography. Note that for all samples listed in this table uranium chemistry was done first after the initial digestion.

Table 4.

The mass-dependent and nucleosynthetic Fe isotopic compositions of the investigated samples and standards.

Sample	Type	Notes	$\delta^{56/54}Fe$	$\varepsilon^{56}Fe$	$\varepsilon^{58}Fe$	$\delta^{56/54}Fe_{corr.}$	2SD	$\varepsilon^{56}Fe_{corr.}$	2SD	$\varepsilon^{58}Fe_{corr.}$	2SD
Egg 2 Plag	Ig	PUC	4.36	0.97	−1.18	4.28	0.05	0.77	0.29	−0.78	1.74
Egg 2 high-Mg Px	Ig	PUC	7.24	1.56	−0.85	7.12	0.05	1.22	0.31	−0.18	1.74
Egg 2 high-Fe Px (dup)	Ig	PUC	9.85	2.34	−0.91	9.66	0.05	1.88	0.33	0.00	2.81
Egg 2 high-Fe Px (dup)	Ig	PUC	9.89	2.38	0.83	9.69	0.08	1.92	0.24	1.74	1.46
164	Ig	PC	−0.84	−0.47	0.52	−0.84	0.08	−0.43	0.24	0.45	1.46
166	FG	PC	−1.57	−0.29	−0.55	−1.57	0.05	−0.22	0.29	−0.69	1.74
167	FG	PC	−1.71	−0.39	0.35	−1.71	0.05	−0.31	0.29	0.19	1.74
168	Ig	PC	0.44	−0.11	0.16	0.44	0.08	−0.13	0.24	0.20	1.46
170	Ig	PC	−0.04	0.03	−0.29	−0.04	0.05	0.04	0.29	−0.30	1.96
171	Ig	PC	−0.47	−0.11	0.91	−0.47	0.06	−0.09	0.29	0.87	1.74
172	Ig	PC	0.38	−0.06	0.67	0.38	0.08	−0.08	0.24	0.70	1.46
173	FG	PC	−0.58	−0.24	0.97	−0.58	0.08	−0.21	0.24	0.92	1.91
174	Ig	PC	0.43	−0.12	1.31	0.43	0.08	−0.14	0.27	1.35	1.46
175	FG	PC	−0.80	−0.02	0.13	−0.80	0.05	0.02	0.29	0.06	2.63
AF01	FG	PC	−1.25	−0.29	−0.23	−1.25	0.05	−0.23	0.29	−0.35	1.74
AF02	FG	PC	−0.44	−0.21	−0.73	−0.44	0.05	−0.19	0.29	−0.77	1.74
AF03	FG	PC	−0.46	−0.17	−0.80	−0.46	0.05	−0.15	0.29	−0.84	1.76
AF04	FG	PC	−0.45	−0.07	−0.77	−0.45	0.05	−0.05	0.29	−0.81	1.74
A-ZH-1	Ig	PC	1.32	0.35	0.67	1.29	0.08	0.28	0.24	0.79	1.95
A-ZH-2	Ig	PC	−0.86	−0.21	0.91	−0.86	0.08	−0.17	0.24	0.83	1.46
A-ZH-3	Ig	PC	−0.38	−0.13	0.23	−0.38	0.08	−0.12	0.24	0.19	1.46
A-ZH-4	Ig	PC	−0.61	−0.21	−0.60	−0.61	0.08	−0.18	0.24	−0.65	1.46
A-ZH-5	FG	PC	−0.46	−0.04	0.77	−0.46	0.08	−0.01	0.24	0.72	1.46
AI01	Ig	PC	0.15	−0.11	−0.38	0.15	0.05	−0.12	0.29	−0.37	2.37
AI02	Ig	PC	−0.52	−0.18	−0.19	−0.52	0.05	−0.16	0.29	−0.23	1.74
Lisa	Ig	PC	0.18	−0.19	0.15	0.18	0.08	−0.20	0.25	0.17	1.46
Marge	Ig	PC	−0.52	−0.26	-	−0.52	0.05	−0.24	0.29	-	-
Bart	Ig	PC	−1.03	−0.34	−0.03	−1.03	0.08	−0.29	0.24	−0.12	1.46
Homer	Ig	PC	−0.04	−0.18	0.42	−0.04	0.08	−0.18	0.24	0.42	1.46
Bulk Allende	chondrite	-	−0.03	−0.13	−0.47	−0.03	0.08	−0.13	0.24	−0.48	1.46
BHVO-2	terrestrial	-	0.10	−0.17	0.47	0.10	0.08	−0.17	0.16	0.47	1.76
BCR-2	terrestrial	-	0.06	0.03	0.79	0.06	0.05	0.03	0.31	0.79	0.94

The $\varepsilon^{56}Fe_{corr.}$ and $\varepsilon^{58}Fe_{corr.}$ have a second-order mass fractionation correction following a Rayleigh distillation as shown by Render et al. (2018). The $\delta^{56/54}Fe_{corr.}$ are corrected for resolved nucleosynthetic anomalies using $\varepsilon^{56}Fe$ (this is only done for Egg 2 mineral separates and A-ZH-1). The uncertainties shown represent either the long-term reproducibility (2SD) based on repeat analyses of the terrestrial standard during the measurement campaign or the 2SD of replicate sample analyses. For Marge, $\varepsilon^{58}Fe$ is not reported due to a large Ni interference in this sample.

Px = pyroxene, Plag = plagioclase, dup = duplicate, Ig = igneous, FG = fine-grained, PUC = previous U ion chromatography only, PC = previous ion chromatography.

Table 5.

The Ti, Ni, and Sr isotopic compositions of the Egg 2 mineral separates.

Sample	Notes	ε^{46}Ti	ε^{50}Ti	ε^{60}Ni	ε^{62}Ni	ε^{64}Ni	ε^{84}Sr	^{87}Sr/^{86}Sr
Egg 2 Plag	PC	1.71	9.37	-	-	-	1.16	0.699084
Egg 2 high-Mg Px	PC	2.33	10.19	-	-	-	1.10	0.699296
Egg 2 high-Fe Px	PC	2.14	9.78	0.78	1.33	2.25	1.60	0.699513
Egg 2 bulk *	PC	-	-	*0.71*	*1.07*	*1.75*	-	-
2SD	-	0.30	0.29	0.08	0.18	0.60	0.50	0.000013

The uncertainties shown represent the long-term reproducibility (2SD) based on repeat analyses of the terrestrial standard during the measurement campaign.

Px = pyroxene, Plag = plagioclase, PC = previously experienced ion chromatography

* Ni isotopic composition of the Egg 2 bulk sample is from Render et al. (2018) and is shown in italics. Given the proportions of the mineral phases in Egg 2, this bulk sample can be considered a mixture of 73 wt.% Ni from Egg 2 high-Fe Px, 16 wt.% Ni from Egg 2 Plag, and 11 wt.% Ni from Egg 2 high-Mg Px.